Coastal Engineering 154 (2019) 103564

Contents lists available at ScienceDirect

Coastal Engineering

journal homepage: http://www.elsevier.com/locate/coastaleng

CFD simulations of violent breaking wave impacts on a vertical wall using a two-phase compressible solver

Shengnan Liu [a], Inno Gatin [b], Charlotte Obhrai [a], Muk Chen Ong [a,*], Hrvoje Jasak [b]

[a] Department of Mechanical and Structural Engineering and Materials Science, University of Stavanger, Stavanger, Norway
[b] Faculty of Mechanical Engineering and Naval Architecture, University of Zagreb, Zagreb, Croatia

ARTICLE INFO

Keywords:
Breaking waves
Air pocket
Impulses
CFD
Compressible flow model

ABSTRACT

Four different types of breaking wave impacts on a vertical wall are simulated using a two-dimensional two-phase Computational Fluid Dynamic (CFD) model. Air is considered as an isentropic ideal gas without solving an additional energy equation and water is treated as an incompressible liquid. The discontinuity in fluid properties across the free surface is treated using the Ghost Fluid Method, which accounts for the jump in density and compressibility. The numerical results are compared with large-scale experimental data for five cases in terms of surface elevations, total forces and pressure distributions along the wall, and a reasonable agreement is obtained overall. The characteristics of impact pressures under different breaking wave conditions are discussed and compared to each other. The two largest total forces on the wall occur in the 'flip-through' and 'large air pocket' cases. The peak pressure of the flip-through impact is localized in both time and space. The pressure within the trapped air pocket is nearly uniform with a smaller peak value and a much longer duration than that of the 'flip-through' case. The compression and expansion of the air pocket results in pressure oscillations, which are overestimated in frequency and amplitude due to the inaccuracy in capturing the air escape. The broken wave case has the smallest total force, but the largest local pressure among the present numerical cases, which demonstrates the necessity to study all different impact types.

1. Introduction

Coastal breakwaters and sea walls can be subjected to extreme wave loads when a wave breaks onto the structure, which can cause severe damage to the coastal steep-fronted structures. Oumeraci (1994) reported that most of the uncertainties during the design process of breakwaters originate from the difficulties to predict the design wave load conditions. Breaking waves are the most significant cause of the damage to breakwaters. This means that the accurate prediction of wave loading is crucial for the engineering design of coastal structures.

The criteria based on the surf similarity parameter cannot define the types of breaking waves properly in the presence of highly reflective obstacles. This is due to the high reflection which can strongly affect the characteristics of breaking. Different shapes of breakers have an important influence on the impact wave load on the structure. Therefore, many researchers have given their own classification of breaking wave loads on vertical structures according to the characteristics of the free surface and the impact pressure, see Kirkgoz (1982); Witte (1988); Chan and Melville (1988); Oumeraci et al. (1993) and Hattori et al. (1994). In general, there are four types of breakers when the waves break on a vertical wall, i.e., the breaker with a slightly inclined surface, the breaker with a vertical front, the plunging breaker with an air pocket, and the broken waves. Kirkgoz (1982) conducted experiments to study breaking wave impacts on vertical walls with different slopes. The largest shock pressures were observed when the wave front was vertical and parallel to the vertical wall, and there was no trapped air between the breaker and the wall. Similar phenomena can be found in Chan and Melville (1988); Cooker and Peregrine (1991b); Kirkgöz (1995) and Kirkgöz and Aköz (2005). This breaking wave condition is called 'flip-through', and the same nomenclature is used in the present study. Lugni et al. (2006) investigated experimentally the flip-through phenomenon excited by a sloshing event inside a small scale tank, which is 1 m long 0.1 m wide and is filled with water up to a height of 0.125 m. It was found that the speed of the jet induced by the flip-through wave impact was about ten times larger than the speed of the approaching wave, and the upward accelerations exceeded 1500*g*. However, a trapped air pocket is also able to produce a large overall force on the wall according to some researchers (Wood et al., 2000; Peregrine et al., 2005; Bullock

* Corresponding author.
E-mail address: muk.c.ong@uis.no (M.C. Ong).

https://doi.org/10.1016/j.coastaleng.2019.103564
Received 5 April 2019; Received in revised form 21 September 2019; Accepted 22 September 2019
Available online 14 October 2019
0378-3839/© 2019 The Authors. Published by Elsevier B.V. This is an open access article under the CC BY license (http://creativecommons.org/licenses/by/4.0/).

et al., 2007). The kinematic and dynamic evolution of the air-pocket wave impact on a liquid tank (see also Lugni et al. (2006)) were investigated by Lugni et al. (2010a, 2010b). The closure of the air pocket and initial compression of the air pocket were considered mainly being influenced by the air leakage flowing out of the air pocket. The subsequent compression and expansion of the air pocket and its movement along the tank were governed by the change of the ambient pressure induced by the hydrodynamic outer flow. Bullock et al. (2007) conducted a large number of large-scale experimental tests of breaking wave impacts on vertical and sloping walls in Groβer Wellen Kanal (GWK). Characteristics of the impact pressures under different breaking wave conditions were discussed in detail. Highest pressures were captured in the flip-through and the trapped air pocket conditions. However, the pressure distribution was not as localized with a trapped air pocket, and the rise time of the wave impact was longer when compared to the flip-through condition. This resulted in a larger total force on the wall with a trapped air pocket than the flip-through condition in some wave periods. Even though the pressures on the wall under a breaker with a slightly inclined surface and a broken wave were not as large as the other breakers, Bullock et al. (2007) suggested that these two types of wave impacts should not be neglected. Their experimental results are also used as validation data in the present numerical study.

The aforementioned studies are mostly based on physical model tests. The aeration plays an important role in the wave impact on a vertical wall (Peregrine et al., 2005; Bredmose et al., 2015). Therefore, scaling effects have a significant influence when the scaling from the model test to the prototype, and this is still an active area of research. Different scaling models (Mitsuyasu, 1967; Takahashi et al., 1985; Cuomo et al., 2010; Bredmose et al., 2015) introduce errors to various degrees during the scaling process. The numerical simulations are therefore a good alternative to the experimental tests without introducing any scaling effects or measurement errors. Simple empirical formulas to estimate wave impact forces on vertical walls can be found in many research papers, such as Minikin (1963); Goda (1975); Blackmore and Hewson (1984); Allsop et al. (1997); Allsop (1999) and Oumeraci et al. (2001). Cooker and Peregrine (1991a, 1995) developed a mathematical model for the ideal wave induced peak pressures on a vertical wall based on "pressure impulse" theory. Zhang et al. (1996) studied the impact of a two-dimensional plunging breaking wave trapping an air pocket against a vertical wall using a mixed-Eulerian-Lagrangian (MEL) scheme based on incompressible potential flow theory. The transient impact process between the plunging breaker and the wall was captured by considering modelling of the trapped air cushion using a polytropic gas law. The simulated maximum impact pressure on the wall agreed reasonably well with the experiments of Chan and Melville (1988). Wood et al. (2000) proposed a "bounce back" model to simulate the trapped air pocket as an oscillating circular air bubble. Their simulation results show a satisfactory agreement with their experimental data. Colagrossi and Landrini (2003) implemented a numerical model based on the incompressible smoothed particle hydrodynamics (SPH) method to deal with a two-dimensional dam-break problem with a vertical wall. The numerical results agree well with CFD simulations using the boundary element method (BEM) and the level set method (LSM). However, the results were unphysical when an air pocket was trapped, which indicated the limitation of their numerical model for violent wave-structure interactions. The numerical model was further improved by Colagrossi et al. (2010) through combining with the moving-least-square (MLS) integral interpolators (Fries and Matthies, 2003). The wave impact with an air pocket on a liquid tank (see also Lugni et al. (2006)) was simulated using the corrected SPH model (cSPH), i.e., an improved numerical model. The cSPH model can help reduce the pressure noise as compared to the results from the SPH model. The damped pressure oscillations and sub-atmospheric pressures after the peak were common features of wave impacts with trapped air and similar behaviour has been observed in previous studies (Oumeraci et al., 1993; Hattori et al., 1994; Walkden et al., 1996); however, these were not captured by the cSPH model in Colagrossi et al. (2010). Nielsen and Mayer (2004) used a single-phase, incompressible solver based on Navier-Stokes (N–S) equations and the volume of fluid (VOF) method to calculate the green water load on ships. Faltinsen et al. (2004) applied BEM for fully nonlinear free surface potential flow to calculate slamming on very large floating structures with a shallow draft. Greco et al. (2007) modelled the green water load on a deck using a coupled two-phase BEM and N–S solver where both air and water phases are incompressible.

When a wave breaks with a trapped air pocket on the vertical wall, the pressure oscillates and these oscillations are related to the compression-expansion of the air pocket (Obhrai et al., 2005). Therefore, air compressibility should be included in the numerical models to correctly simulate wave impacts with entrapped or entrained air. Gómez-Gesteira and Dalrymple (2004) modelled a dam break generated wave on a prism structure with a three-dimensional SPH method. Numerical velocities and forces were in good agreement with their laboratory measurements. Bredmose et al. (2009) proposed a coupled model to deal with the breaking wave impacts on a vertical wall including the aeration effects. The model combined a weakly compressible flow model for the air phase and potential flow theory for the water phase. Their numerical model was used to reproduce the flip-through and the trapped air pocket cases from Bullock et al. (2007). However, due to the assumptions of the potential flow, the flow details could not be captured properly. The broken wave case was not able be reproduced using their numerical model due to the fact that the turbulence effects were not considered. Plumerault et al. (2012) and Ma et al. (2014) developed their two-phase compressible models based on a multi-phase N–S approach. Good accuracy was shown for wave breaking during shock wave propagation (Plumerault et al., 2012). Several basic test cases were presented in Ma et al. (2014) including a gravity-induced liquid piston motion, a free drop of a two-dimensional water column, water-air mixture shock tubes, water entry of a flat plate, and a plunging wave impact on a vertical wall. However, the simulated plunging wave-induced pressure were not validated by experimental data. Wemmenhove et al. (2015) investigated internal wave loading using ComFLOW method (Veldman et al., 2011, 2014). The N–S equations were solved and a newly-developed gravity-consistent density averaging method was applied to prevent spurious velocities around the free surface. The experimental pressure on a LNG tank section was compared with both single-phase (water phase) and two-phase (incompressible water and compressible air) simulations during the impact involving the trapped air pocket. The comparison showed that the single phase model overestimated the pressures significantly. The two-phase modelling and compressibility effects can be beneficial for simulating wave loading.

To the authors' knowledge, very few numerical studies have been published on violent breaking wave impacts on a vertical wall or other steep-fronted structures. There is no numerical study which has simulated all the aforementioned four different types of breaking wave-wall structure interactions completely. In the present study, a two-dimensional two-phase CFD model is used to simulate different breaking wave impacts on a vertical wall, which models air phase as an isentropic ideal gas and water as an incompressible phase. Mesh and time-step refinement studies are conducted based on the comparisons of surface elevations at four wave gauges. The characteristics of impact pressures on the vertical wall under different impact conditions are studied in detail. The numerical surface elevations, total forces and pressure distributions are compared to the experimental data of Bullock et al. (2007). The discrepancies between the simulation and the experiment will be discussed.

2. Numerical implementation

The numerical simulations are conducted using foam-extend 4.0 (Jasak et al., 2015). The numerical implementation is presented in this

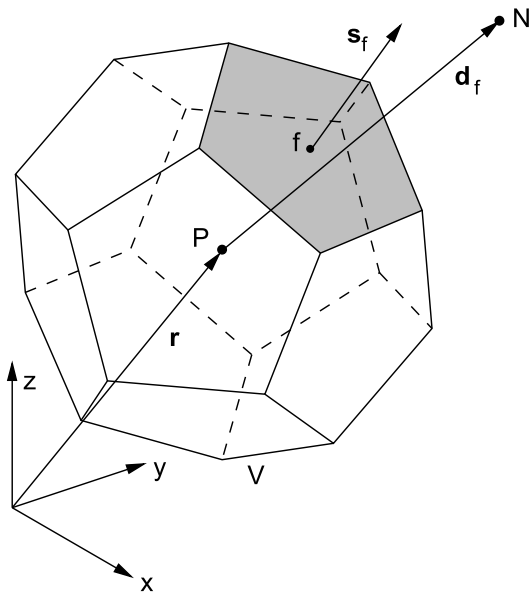

Fig. 1. Schematic representation of a polyhedral control volume P, which shares a face *f* with its immediate neighbour *N*.

section including governing equations, free surface modelling, turbulence models and boundary conditions.

2.1. Governing equations and free surface capturing

A two-phase, immiscible, viscous and turbulent flow is considered, where the air phase is assumed to be an ideal gas undergoing adiabatic compression/expansion, while water is modelled as an ideally incompressible liquid. Under the aforementioned assumptions, the momentum conservation equation becomes:

$$\frac{\partial \mathbf{u}}{\partial t} + \nabla\cdot(\mathbf{uu}) - \nabla\cdot(\mathbf{R}) = -\frac{1}{\rho}\nabla p_d - \left(\frac{1}{\rho}\nabla\rho\mathbf{g}\cdot\mathbf{x} - \mathbf{u}\nabla\cdot\mathbf{u}\right), \quad (1)$$

where **u** denotes the velocity field, ρ stands for the discontinuous density field and **R** presents the Reynolds stress tensor, allowing general turbulence modelling. p_d stands for the dynamic pressure calculated as $p_d = p - \rho\mathbf{g}\cdot\mathbf{x}$, where p denotes the static pressure, **g** is the gravity vector, while **x** denotes the radii vector. For two-phase flow, the volume fraction follows $\alpha_c = 1 - \alpha_I$, and density $\rho = \alpha_I\rho_I + (1 - \alpha_I)\rho_c$, where the subscript I is for the incompressible phase and c is for the compressible phase. The momentum and mass conservation equations for two phase flow can be written as:

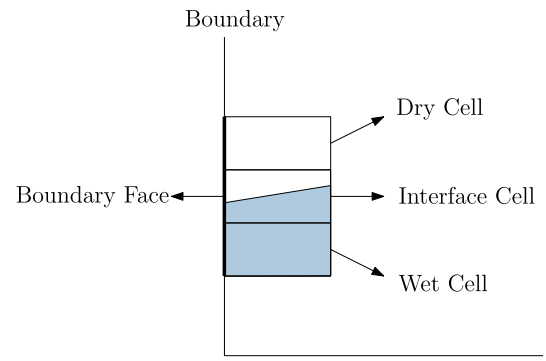

Fig. 3. Sketch of different types of computation cells at the inlet boundary.

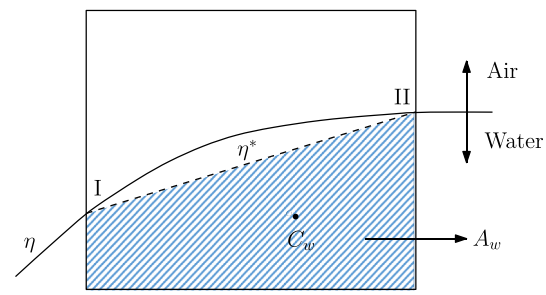

Fig. 4. Sketch of velocity condition on the interface cell with $0 < \alpha < 1$.

Table 1
Summary of the simulated cases.

Case index	Water depth d (m)	Water depth at wall d_w (m)	Wave period T (s)	Wave height H (m)	Impact type
1	4.25	1.25	6	1.35	slightly-breaking
2	4.25	1.25	7	1.35	flip-through
3	4.02	1.02	8	1.10	small air pocket
4	4.00	1.00	8	1.25	large air pocket
5	3.70	0.70	8	1.00	broken

Table 2
Positions of the wave gauges.

No.	WG1	WG2	WG3	WG4	WG5	WG6
x (m)	−156.14	−13.29	−9.29	−5.29	−2.14	−0.02

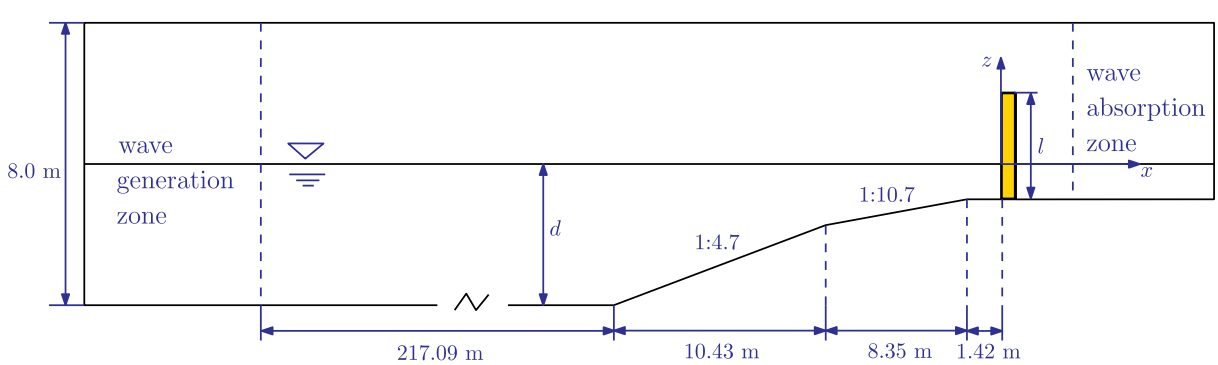

Fig. 2. Sketch of the numerical wave tank and the coordinate system.

Table 3
Vertical positions of the pressure transducers in the numerical simulations and the experiment.

No.	P1	P2	P3	P4	P5	P6	P7	P8	P9	P10
z_1 (m)	3.48	3.73	4.03	4.38	4.53	4.73	4.93	5.13	5.53	5.88
z_2 (m)	3.65	3.90	4.20	4.55	4.70	4.90	5.10	5.30	5.70	6.55

Table 4
Grid resolutions for the plunging breaker case.

Mesh index	M1	M2	M3	M3*	M4
Total number of cells	155180	281476	464610	464610	578240
Number of cells per wavelength	260	360	520	520	610
Number of cells per wave height	12	24	36	36	48
Maximum Courant number	0.5	0.5	0.5	0.3	0.5

$$\frac{\partial \mathbf{u}}{\partial t} + \nabla\cdot(\mathbf{uu}) - \frac{1}{\rho}\nabla\mathbf{u}\cdot\nabla\mu_e - \frac{1}{\rho}\nabla\cdot(\mu_e\nabla\mathbf{u}) = -\frac{1}{\rho}\nabla p_d - (1-\alpha_I)\left(\frac{1}{\rho_c}\nabla\rho_c\mathbf{g}\cdot\mathbf{x} - \mathbf{u}\nabla\cdot\mathbf{u}\right). \tag{2}$$

$$\nabla\cdot\mathbf{u} = -(1-\alpha_I)\frac{1}{\rho_c}\frac{\partial\rho_c}{\partial p}\left(\frac{\partial p_d}{\partial t} + \nabla\cdot(p_d\mathbf{u}) - p_d\nabla\cdot\mathbf{u} + \frac{\partial(\rho_c\mathbf{g}\cdot\mathbf{x})}{\partial t} + \mathbf{u}\cdot\nabla\rho_c\mathbf{g}\cdot\mathbf{x}\right). \tag{3}$$

The relation between density and pressure for the ideal isentropic gas is expressed by the following equation:

$$\frac{\partial\rho_c}{\partial p} = \frac{1}{a_c\gamma}\frac{p}{a_c}^{\frac{1-\gamma}{\gamma}}, \tag{4}$$

where γ denotes the constant specific heat ratio while a_c is the isentropic constant. In this paper, the values of $\gamma = 1.4$ and $a_c = 100\,000$ are used.

Finite Volume (FV) method is used to discretise governing equations, i.e., Equations (2) and (3) (Jasak and Gosman, 2001). The present notation adheres to Vukčević et al. (2017), as shown in Fig. 1: $\mathbf{s}_f$ is the surface area vector of a face; $\mathbf{d}_f$ stands for the vector from the cell centre P to the cell centre N, where P and N represent two adjacent cells that share a face. Terms enclosed in curly braces $\{\cdot\}$ indicate that implicit FV discretisation is used, while explicit evaluation is used for the remaining terms.

Equation (2) can be discretised as:

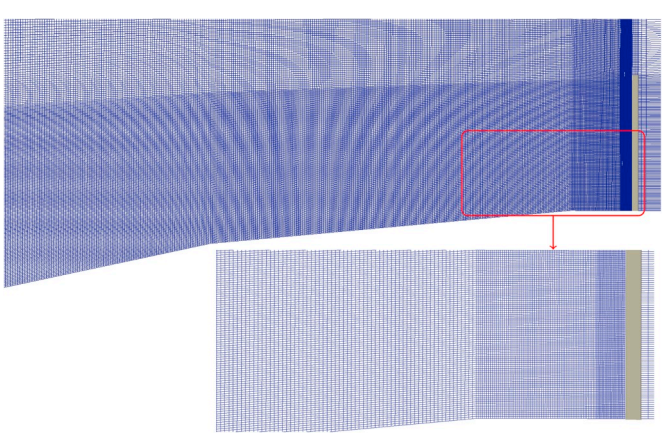

Fig. 5. Mesh of the vicinity of the vertical wall (top), zoom-in view of the mesh around the vertical wall (bottom).

$$\left\{\frac{\partial\mathbf{u}}{\partial t}\right\} + \{\nabla\cdot(\mathbf{uu})\} - \left\{\frac{1}{\rho}\nabla\mathbf{u}\cdot\nabla\mu_e\right\} - \left\{\frac{1}{\rho}\nabla\cdot(\mu_e\nabla\mathbf{u})\right\} = -\frac{1}{\rho}\nabla p_d - (1-\alpha_I)\left(\frac{1}{\rho_c}\nabla\rho_c\mathbf{g}\cdot\mathbf{x} - \{\mathbf{u}\nabla\cdot\mathbf{u}\}\right). \tag{5}$$

The temporal and viscous terms are continuous across the interface, where the special treatment is not needed. The convection, dynamic pressure gradient, density gradient and $\mathbf{u}\cdot\nabla\mathbf{u}$ terms require the special treatment when calculated across the interface. For the conservation of mass, the discretised form of Equation (3), can be written as:

$$\{\nabla\cdot\mathbf{u}\} = -(1-\alpha_I)\frac{1}{\rho_c}\frac{\partial\rho_c}{\partial p}\left(\left\{\frac{\partial\rho_d}{\partial t}\right\} + \{\nabla\cdot(p_d\mathbf{u})\} - \{p_d\nabla\cdot\mathbf{u}\} + \frac{\partial(\rho_c\mathbf{g}\cdot\mathbf{x})}{\partial t} + \mathbf{u}\cdot\nabla\rho_c\mathbf{g}\cdot\mathbf{x}\right). \tag{6}$$

Due to the discontinuities across the free surface, all terms in Equation (6) require the special treatment stated as follows. The pressure equation is obtained from Equation (6) following Jasak (1996). The discretised left hand side of the conservation of mass, Equation (6), in integral form is:

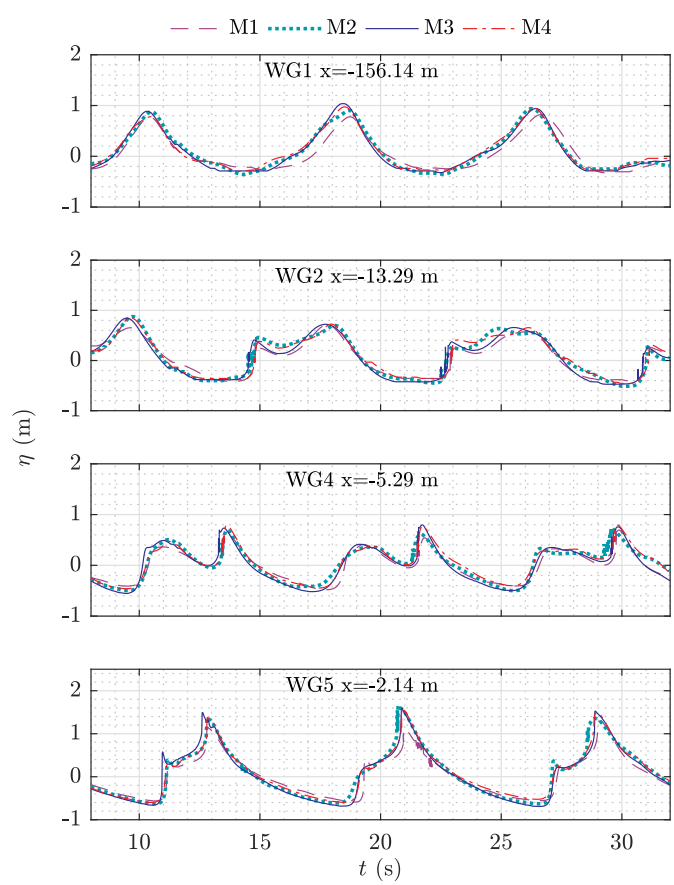

Fig. 6. Surface elevations at different wave gauges with different grid resolutions.

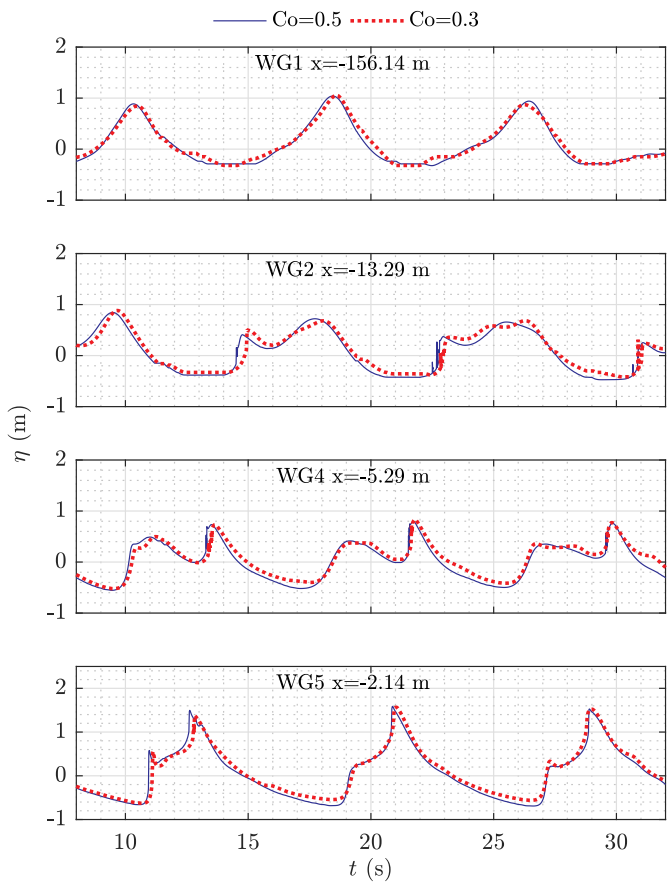

Fig. 7. Surface elevations at different wave gauges with different maximum Courant numbers.

$$\int_{CV} \nabla\cdot\mathbf{u}\,\mathrm{d}V = \int_{\partial CV} \mathrm{d}\mathbf{s}\cdot\mathbf{u} = \sum_f \mathbf{s}_f\cdot\mathbf{u}_f, \tag{7}$$

where CV stands for the control volume, V is the cell volume, f is the control volume face index, $\mathrm{d}\mathbf{s}$ is the infinitesimal surface normal vector, and $\mathbf{s}_f$ stands for the face area vector. Cell-centred velocity is expressed

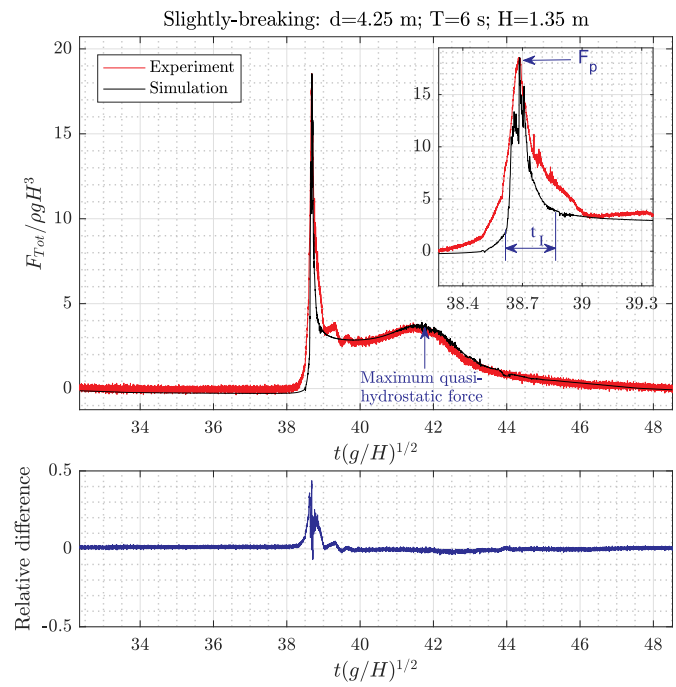

Fig. 9. Comparison of the simulated and experimental wave forces on the vertical wall for Case 1: d = 4.25 m; T = 6 s; H = 1.35 m, F_p = 18.54 (447.6 kN), t_l = 0.24 (88.5 ms).

by using the semi-discretised form of the momentum equation:

$$\mathbf{u}_P = \frac{\mathbf{H}(\mathbf{u}_N)}{a_P} - \frac{1}{\rho a_P}(\nabla p_d + \nabla\rho\mathbf{g}\cdot\mathbf{x}), \tag{8}$$

where a_P denotes the summed diagonal coefficient for cell P, while $\mathbf{H}(\mathbf{u}_N)$ represents a linearised operator containing off-diagonal and source contribution resulting from the discretisation of implicit velocity operators. In order to substitute face centred velocity $\mathbf{u}_f$ using Equation (8), it must be interpolated to cell faces:

$$\mathbf{u}_f = \frac{(\mathbf{H}(\mathbf{u}_N))_f}{(a_P)_f} - \left(\frac{1}{a_P}\right)_f \left(\frac{1}{\rho}\right)_{fr} \left((\nabla p_d)_{fr} + (\nabla\rho)_{fr}\mathbf{g}\cdot\mathbf{x}\right), \tag{9}$$

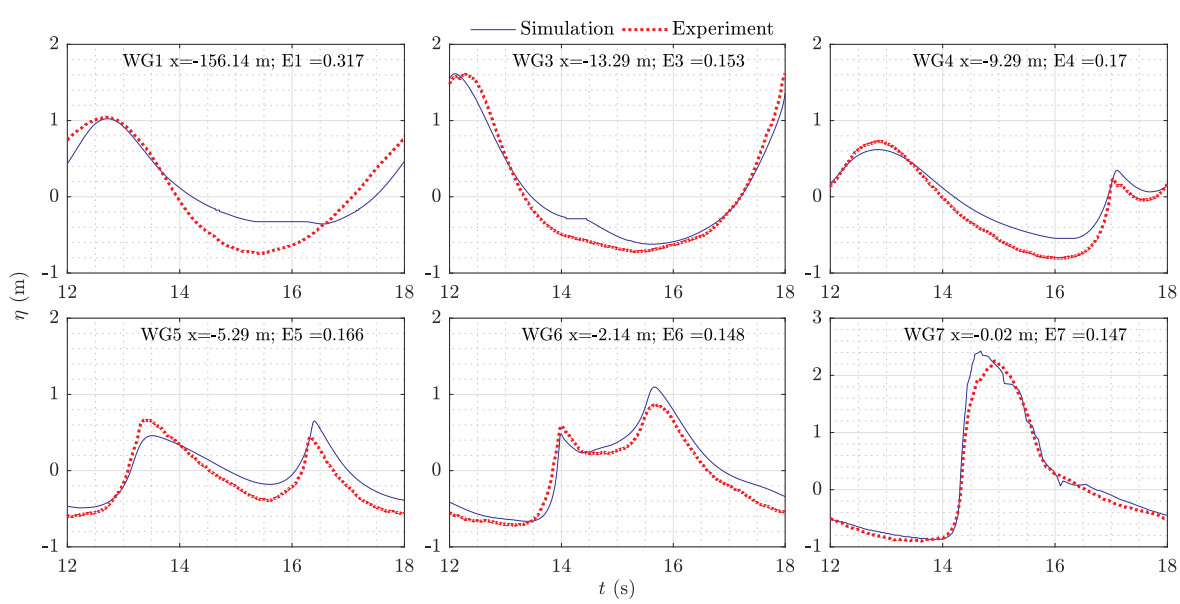

Fig. 8. Comparison of simulated and experimental surface elevations at different wave gauges for Case 1: d = 4.25 m; T = 6 s; H = 1.35 m.

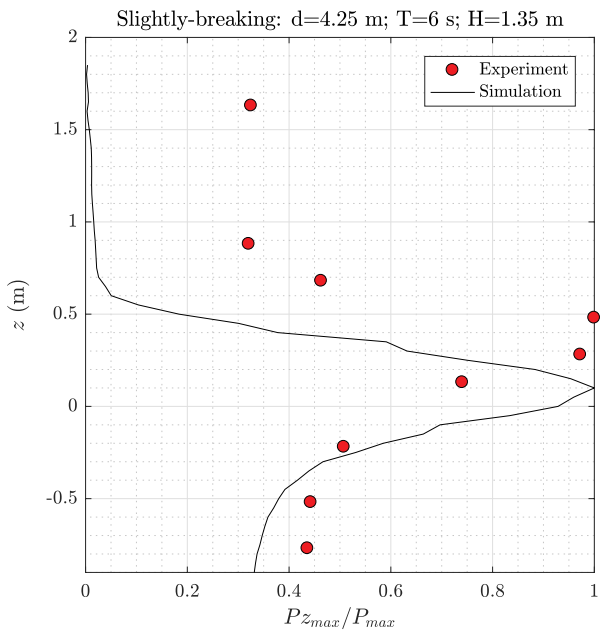

Fig. 10. Comparison of the simulated and experimental maximum pressure along the vertical wall for the slightly-breaking case.

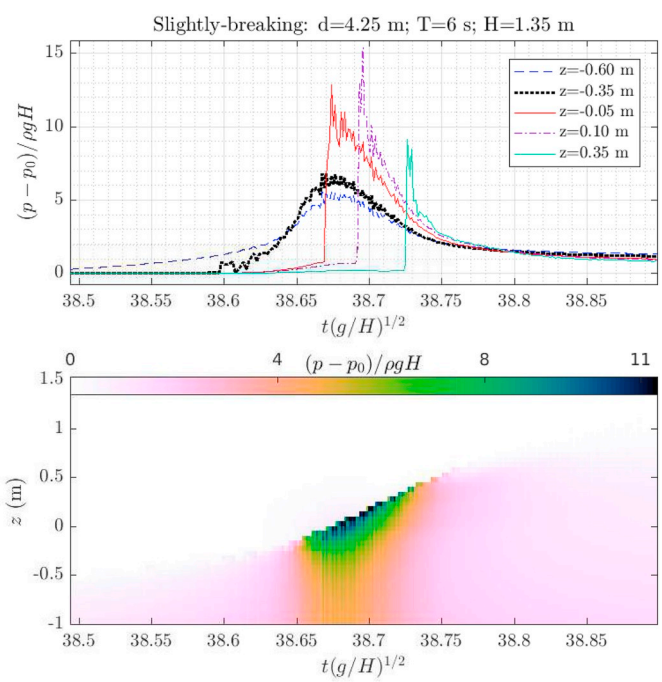

Fig. 11. Pressure variation and distribution along the vertical wall during an impact for Case 1: d = 4.25 m; T = 6 s; H = 1.35 m.

where index f_Γ denotes terms that need special attention across the interface. By substituting Equation (9) into Equation (7), the discretised conservation of mass can be written as:

$$\sum_f \mathbf{s}_f \cdot \left(\frac{1}{a_P}\right)_f \left(\frac{1}{\rho}\right)_{f_\Gamma} (\nabla p_d)_{f_\Gamma} = \sum_f \mathbf{s}_f \cdot \left(\frac{(\mathbf{H}(\mathbf{u}_N))_f}{(a_P)_f} - \left(\frac{1}{\rho}\right)_{f_\Gamma} (\nabla \rho)_{f_\Gamma} \mathbf{g}\cdot\mathbf{x}\right) + \int_{CV} f_C(p_d, \rho)\mathrm{d}V, \tag{10}$$

where

$$f_C(p_d, \rho) = -(1-\alpha_I)\frac{1}{\rho_c}\frac{\partial \rho_c}{\partial p}\left(\left\{\frac{\partial p_d}{\partial t}\right\} + \{\nabla\cdot(p_d\mathbf{u})\} - \{p_d \nabla\cdot\mathbf{u}\} + \frac{\partial(\rho_c \mathbf{g}\cdot\mathbf{x})}{\partial t} + \mathbf{u}\cdot\nabla\rho_c\mathbf{g}\cdot\mathbf{x}\right). \tag{11}$$

In the present numerical framework, the Ghost Fluid Method (GFM) (Desjardins et al., 2008; Huang et al., 2007; Queutey and Visonneau, 2007) is used to implicitly account for the abrupt change in fluid properties across the interface, and to satisfy the free surface boundary conditions. Additional equations describing the jump conditions are derived, and they need to be satisfied along with the governing equations. The jump conditions are embedded into the solution process via specialised discretisation schemes that are used for operators near the free surface. By employing the GFM, the terms in Equations (2) and (3) responsible for compression have a sharp change in value across the interface. That means that for a cell adjacent to the interface on the water side, the last term in Equation (2) and the right hand side of Equation (3) are equal to zero, since $\nabla\rho = 0$, $\nabla\cdot\mathbf{u} = 0$, and $\partial\rho/\partial p = 0$ for incompressible phase. For a cell on the air side next to the interface, these terms are fully evaluated, giving a complete compressible model. This approach is different from most numerical models where the compressibility properties are blended using the volume fraction field. The present implementation including the compressible air phase is an extension of the existing incompressible numerical model with GFM developed by Vukčević et al. (2017), who reported that the approach removes the spurious air velocity problems near the interface.

From the dynamic free surface boundary condition the following jump condition arises:

$$[p] = p^- - p^+ = 0, \tag{12}$$

stating that the pressure needs to be equal on both sides of the interface. Here, $[\cdot]$ denotes the jump operator, + and − indices denote the value infinitesimally close to the interface from the water side and air side, respectively. When written in terms of the dynamic pressure, the above equations reads:

$$[p_d] = -[\rho]\mathbf{g}\cdot\mathbf{x}, \tag{13}$$

which in effect states that the dynamic pressure has a jump across the interface. The kinematic free surface boundary condition states that the velocity must be continuous across the interface:

$$[\mathbf{u}] = \mathbf{u}^- - \mathbf{u}^+ = 0 \tag{14}$$

Apart from the two jump conditions arising directly from the free surface boundary conditions, additional conditions arise from the governing equations (Desjardins et al., 2008; Huang et al., 2007; Queutey and Visonneau, 2007). The jump condition arising from the momentum equation (Equation (2)) states:

$$\left[\frac{1}{\rho}\nabla p_d\right] = \left[-\nabla\cdot(\mathbf{u}\mathbf{u}) + \mathbf{u}\nabla\cdot\mathbf{u} - \frac{1}{\rho}\nabla\rho\mathbf{g}\cdot\mathbf{x}\right] \tag{15}$$

Equation (15) shows that the dynamic pressure gradient divided with the discontinuous density field has a jump related to the compressibility of the gas phase. Note that if there are no compressible effects, the right hand side of Equation (15) reduces to zero, correctly yielding the expression for incompressible flow reported byVukčević et al. (2017).

In addition to above mentioned jump conditions, the jump in density also needs to be taken into account:

$$[\rho] = \rho^- - \rho^+, \tag{16}$$

where ρ^+ is constant, while ρ^- needs to be calculated. Since the air is considered as an adiabatic ideal gas, the following holds:

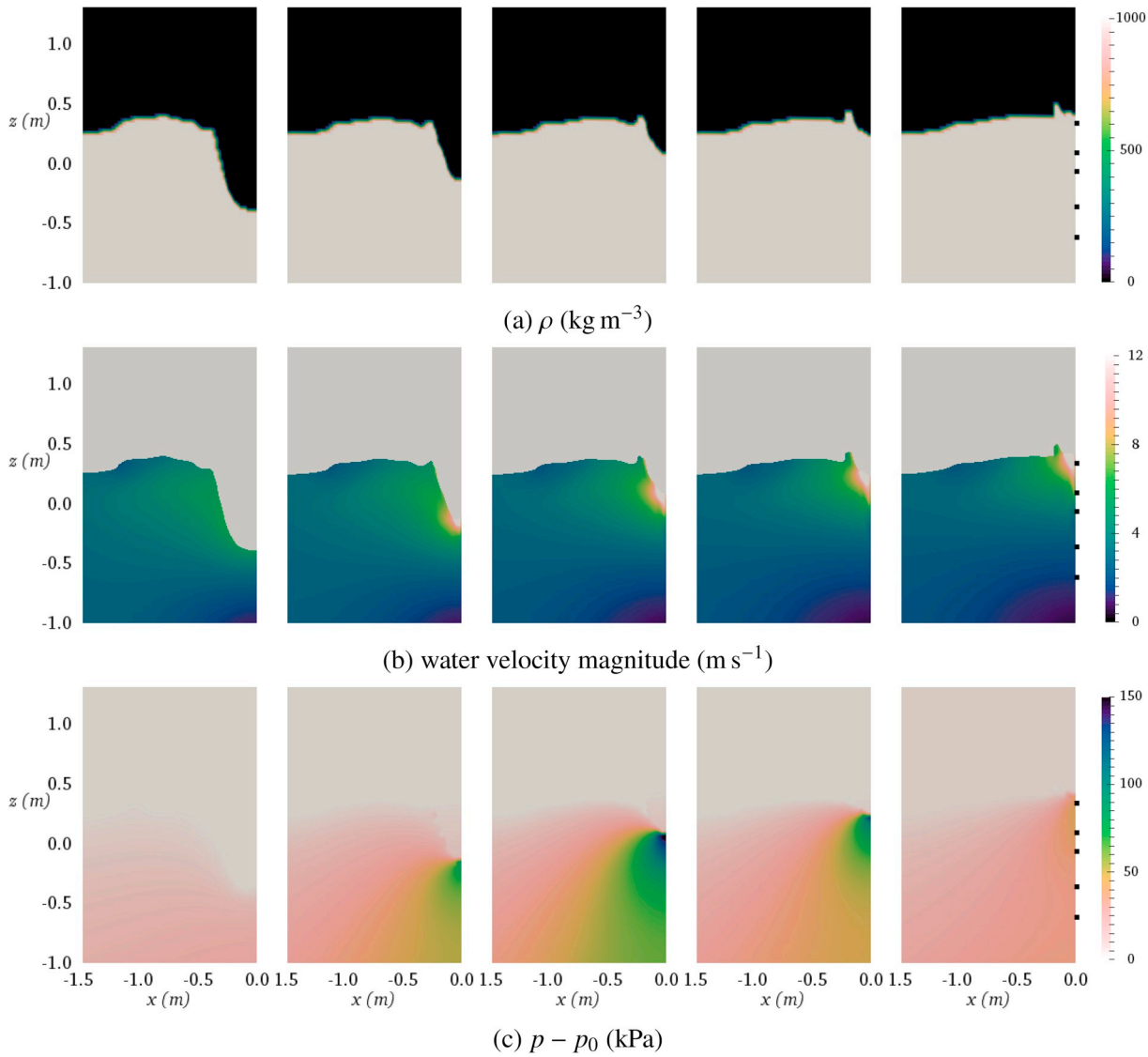

Fig. 12. Density, water velocity magnitude and pressure variations at different time instants during one impact for Case 1: d = 4.25 m; T = 6 s; H = 1.35 m, from left to right: $t_1 = 38.57$, $t_2 = 38.65$, $t_3 = 38.68$, $t_4 = 38.70$ and $t_5 = 38.73$.

$$\rho^- = \left(\frac{p^-}{a_c}\right)^{\frac{1}{\gamma}} = \left(\frac{p_d^- + \rho^- \mathbf{g}\cdot\mathbf{x}}{a_c}\right)^{\frac{1}{\gamma}} \tag{17}$$

The presented equations form a closed system describing a two–phase flow model with an incompressible liquid phase and an ideal gas phase undergoing adiabatic compression/expansion. Readers are referred to Gatin (2018) for details regarding the implementation of the present model, while the implementation of the GFM for incompressible two phase flow can be found in Vukčević et al. (2017).

In this work, interface capturing is performed using the isoAdvector (Roenby et al., 2016) method, which is a geometric VOF approach. The isoAdvector provides a sub–grid resolution of the free surface giving superior definition of the free surface in violent impact events. Readers are referred to Roenby et al. (2016) for further details.

2.2. Relaxation method

The wave relaxation method presented by Jacobsen et al. (2012) is employed to generate waves in the inlet relaxation zone and absorb waves in the outlet relaxation zone. Inside the relaxation zones, the relaxation function γ_R is applied with the expression of:

$$\gamma_R = 1 - \frac{exp(\chi_R^{3.5}) - 1}{exp(1) - 1}, \tag{18}$$

$$\varphi = \gamma_R \varphi_{computed} + (1 - \gamma_R)\varphi_{target}, \tag{19}$$

where φ is either the velocity vector **u** or the volume fraction α, $\chi_R \in [0, 1]$, $\gamma = 1$ at the interface between the working zone and the relaxation zones. The values in the relaxation zones ramp up to the target values, which depend on the selected wave theory in the inlet relaxation zone whereas they are zero in the outlet relaxation zone. In the present study, the inlet and outlet relaxation zones are one wavelength long.

2.3. Turbulence modelling

Free surface $k - \omega$ SST turbulence model (FS $k - \omega$ SST) is implemented and used in the present study. The basic idea of the FS $k - \omega$ SST is to use a laminar regime around the free surface to prevent overprediction of wave damping. The laminar layer around the free surface can be controlled precisely and the k value in the surf zone can be

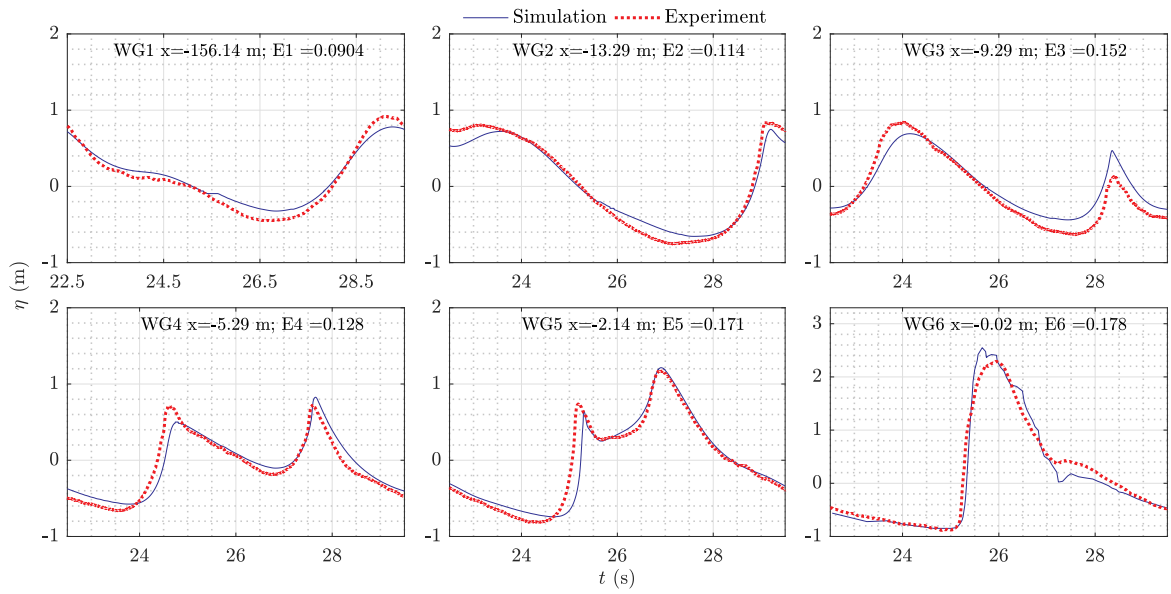

Fig. 13. Comparison of simulated and experimental surface elevations at different wave gauges for Case 2: d = 4.25 m; T = 7 s; H = 1.35 m.

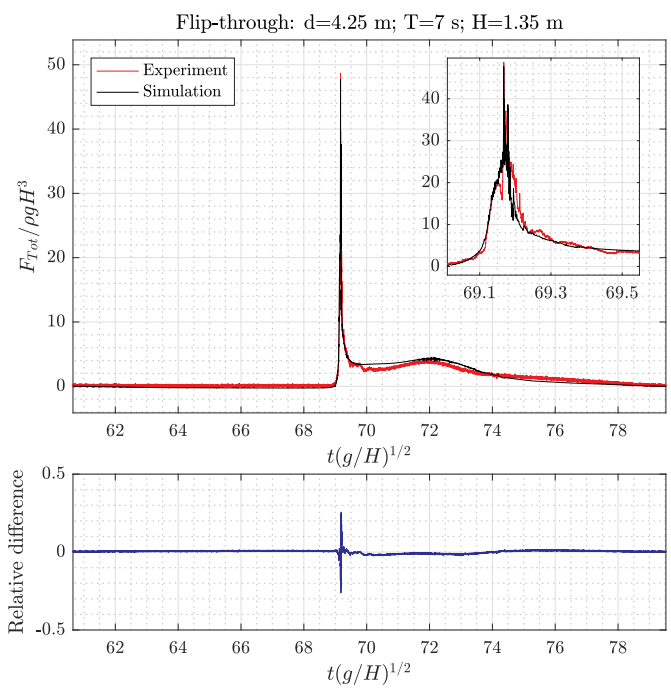

Fig. 14. Comparison of the simulated and experimental wave forces on the vertical wall for Case 2: d = 4.25 m; T = 7 s; H = 1.35 m, $F_p = 47.68$ (1 150.8 kN), $t_I = 0.03$ (11.6 ms).

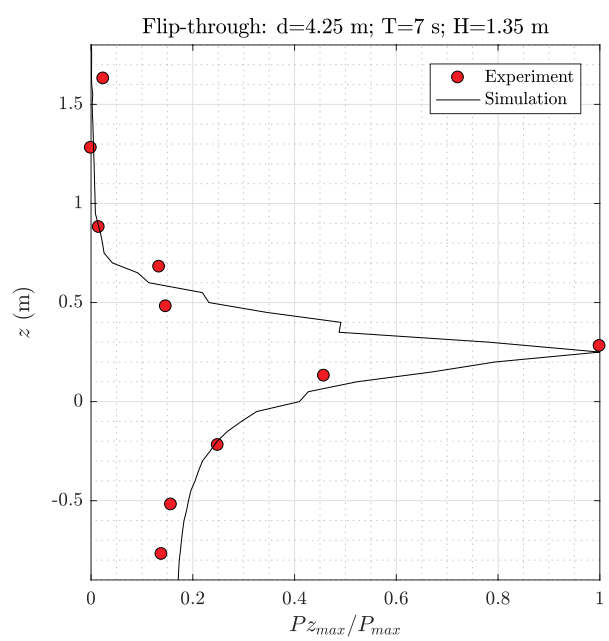

Fig. 15. Comparison of the simulated and experimental maximum pressures along the vertical wall for the flip-through case.

predicted reasonably. The forms of the transport equations for k and ω are the same as the original $k-\omega$ SST turbulence model (see more information in Menter (1994)):

$$\frac{\partial k}{\partial t}+\nabla\cdot(\mathbf{u}k)-P_k+\beta^* k\omega-\nabla\cdot[(\nu+\sigma_k\nu_T)\nabla k]=T(k)=0, \tag{20}$$

$$\frac{\partial \omega}{\partial t}+\nabla\cdot(\mathbf{u}\omega)=\delta S^2-\beta\omega^2+\nabla\cdot[(\nu+\sigma_\omega\nu_T)\nabla\omega]+2(1-F_1)\frac{\sigma_{\omega 2}}{\omega}\nabla k\cdot(\nabla\omega)^T, \tag{21}$$

where $T(k)$ is the implicit form of the transport equation for k. The term k is blended implicitly with a function γ to obtain a laminar region in the vicinity of the free surface:

$$\begin{aligned}&\gamma T(k)+(k_{FS}-k)(1-\gamma)=0,\\&k_{FS}=\frac{\beta_l\nu_l\max(a_1\omega,SF_2)}{a_1},\\&\gamma=\max\left(\frac{\psi_l}{l_b},1\right),\end{aligned} \tag{22}$$

where k_{FS} is the turbulent kinetic energy around the free surface; $\beta_l = \nu_T/\nu_l$ is the ratio between the turbulent eddy viscosity and the laminar viscosity; $\gamma=\gamma(\mathbf{x},t)$ approaches zero around the free surface. The

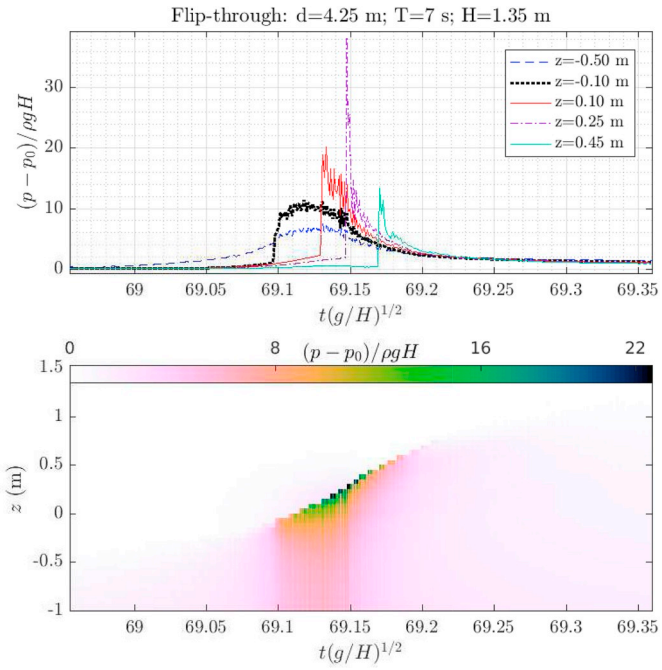

Fig. 16. Pressure variation and distribution along the vertical wall during an impact for Case 2: d = 4.25 m; T = 7 s; H = 1.35 m.

original transport equation for k is recovered when it is away from the free surface, i.e., $\gamma = 1$. The term ψ_l is the incident level set field defined as the least distance towards the incident free surface, which is employed to guarantee numerical stability where the total level set field has a distortion. The term l_b is the user-defined blending length, which represents the distance from the free surface where the target viscosity (laminar viscosity in the present study) is imposed. The term l_b should be as small as possible to ensure that the laminar region is confined to the vicinity of the free surface, which is around one cell height in the present study.

2.4. Computational domain and boundary conditions

The experimental data used for the validation study were breaking wave impacts on a vertical wall conducted by Bullock et al. (2007) at a model scale of 1:4. The tests were performed in GWK and wave pressures were measured with a sampling frequency of 10 kHz. More details of the experimental tests can be found in Bullock et al. (2007).

The present two-dimensional computational domain is set up according to the experimental arrangements, and the layout of the numerical wave tank is presented in Fig. 2. The origin of the coordinate system is at the intersection point of the front face of the vertical wall and the still water line. The distance between the end of the wave generation zone and the vertical wall is 237.29 m, which is consistent with the distance between the wave maker and the vertical wall in the experiment. Two different bottom slopes connect to each other in front of the wall, and the slope values match the slope profiles in the experiments. The incident waves in the numerical wave tank are generated based on non-linear stream function theory (Dean, 1965).

Fig. 3 shows three different states for the computational cells adjacent to the domain boundary, i.e. completely in the water (wet cell), completely in the air (dry cell), and intersected by the free surface (interface cell). For interface cells, I and II are the intersection points, η^* is the linear approximation to the real free surface η, see Fig. 4. The shaded part represents the wet area A_w. The wet geometry centre point is C_w, and α at the boundary is defined as A_w/A, where A is the area of the boundary face.

The boundary conditions used in the present computational domain are shown as follows:

(i) Inlet boundary: the boundary conditions for the dry boundary cells are:

$$\mathbf{n}\cdot\nabla p_{rghair} = 0, \qquad \mathbf{u} = 0, \qquad \alpha = 0 \tag{23}$$

the boundary conditions for the wet boundary cells are:

$$\mathbf{n}\cdot\nabla p_{rghwater} = 0, \qquad \mathbf{u} = \mathbf{u}_{wave}(x,z,t), \qquad \alpha = 1 \tag{24}$$

where $\mathbf{n}$ is the unit normal vector to the boundary cell; p_{rghair} and $p_{rghwater}$ are the pressures in excess of the static pressure in air and water, respectively. The $\mathbf{u}_{wave}(x,z,t)$ is the velocity according to the chosen wave theory. The boundary conditions for the interface cells can be obtained from Equation (24) and applied at the C_w point. The turbulence terms k and ω are calculated according to Menter (1994).

(ii) Outlet boundary: p_{rgh}, k and ω are prescribed with the normal zero-gradient boundary condition, and $\mathbf{u} = \mathbf{0}$ is applied along the boundary.

(iii) Top boundary: the top of the computational domain is a free boundary which allows air and water to flow out freely and only air to flow in. A normal zero-gradient boundary condition is applied for the outflow velocity. For the inflow, the velocity is obtained from the flux in the patch-normal direction. The pressure at the top boundary is set as 'total pressure', which is calculated by:

$$p_T = p_0 - 0.5\mathbf{u}^2 \tag{25}$$

where p_T is the total pressure, p_0 is the reference pressure and is set as 0 at the top boundary. The normal zero-gradient boundary condition is also applied for k and ω at the top boundary.

(iv) Vertical wall and bottom: a no-slip wall boundary condition is used on the vertical wall and the bottom. The fluid velocities at the boundary are zero. The normal zero-gradient boundary condition is applied for p_{rgh}.

2.5. Numerical scheme

Equations are solved with the Finite Volume Method (Versteeg and Malalasekera, 2007) approach and the PIMPLE (pressure-implicit method for pressure-linked equations) (Holzmann, 2017). The convection terms, the diffusion terms and the gradient terms are discretised by second-order Gauss scheme with Gamma differencing (Jasak et al., 1999), second-order limited Gauss linear scheme and second-order face-limited Gauss scheme (Jasak, 2009), respectively. Second-order backward scheme is used for time discretisation. Special treatment for dynamic pressure across the interface can be seen in Gatin (2018).

3. Results and discussion

There are four distinct types of wave impacts on a vertical wall as mentioned previously. A summary of different types of wave impacts is given as follows:

(i) Slightly-breaking: the wave does not break before reaching the wall and hits the wall with a slightly inclined surface.
(ii) Flip-through: the wave breaks exactly on the wall with a nearly vertical wave front as it impacts the wall.
(iii) Trapped air pocket: two different types of trapped air pocket are included, i.e., a plunging breaker entraps a small air pocket located higher on the wall; a well-developed plunging breaker entraps a larger air pocket.

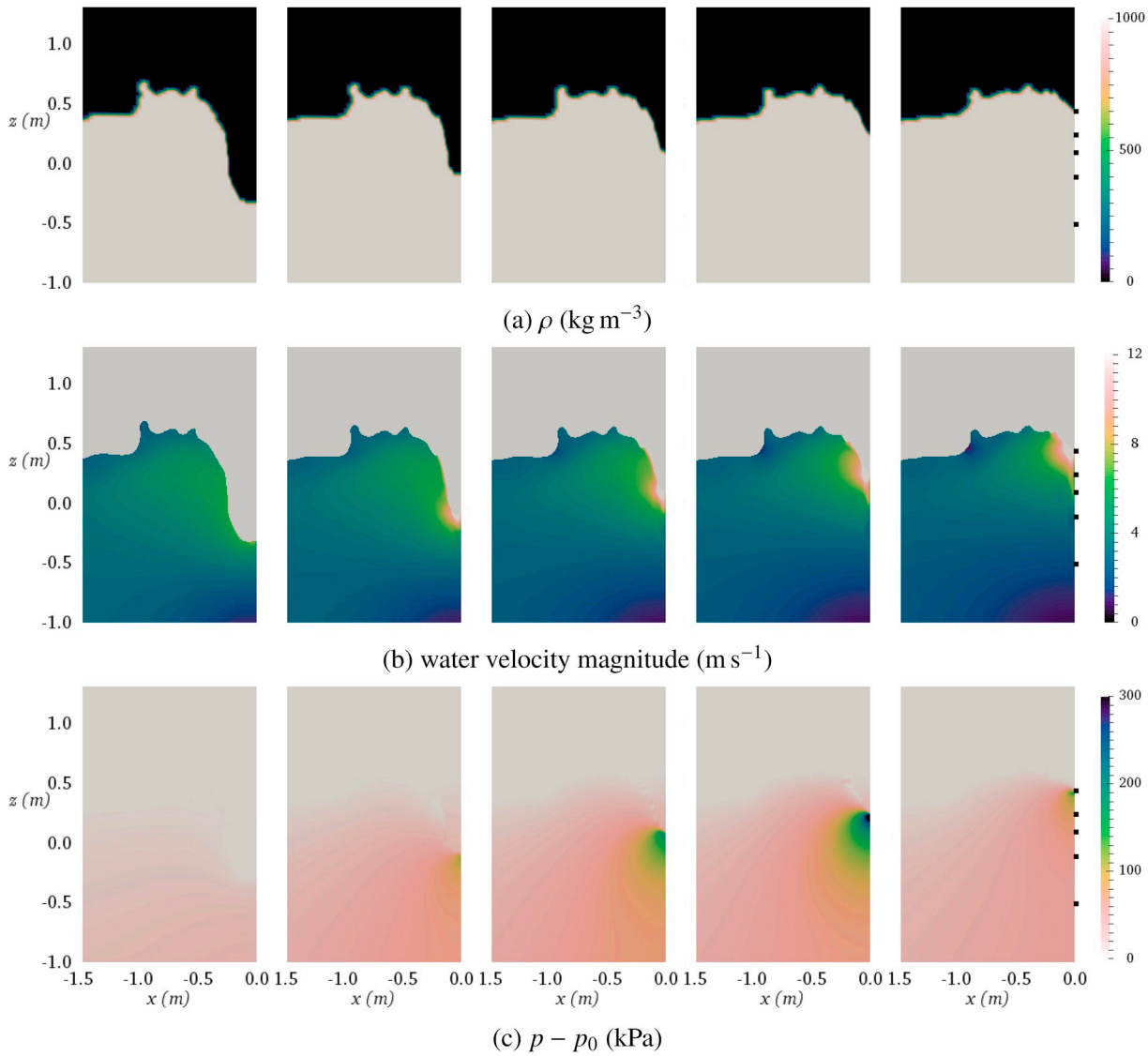

Fig. 17. Density, water velocity magnitude and pressure variations at different time instants during one impact for Case 2: d = 4.25 m; T = 7 s; H = 1.35 m, from left to right:$t_1 = 69.07$, $t_2 = 69.13$, $t_3 = 69.14$, $t_4 = 69.16$ and $t_5 = 69.18$.

(iv) Broken: the wave already breaks before the wall and hits the wall with a turbulent foamy bore.

The distance between the breaking point and the wall increases from the slightly-breaking to the broken wave case. Five simulation cases are presented which corresponds to the different impact types, as shown in Table 1. There were many test cases in the experimental study (Bullock et al., 2007) under different incident waves. The most severe cases for each impact type were selected for use in the present study.

Table 2 gives the x coordinates of six wave gauges along the numerical wave tank. WG1 is in the flat region before the slope. WG2 to WG5 are located at different locations along the two slopes, WG6 is 2 cm in front of the vertical wall.

In the experiment, ten pressure transducers were installed on the wall in a vertical array. The vertical distances between the pressure transducers and the flat bottom in the present numerical simulations are shown in Table 3, and are consistent with the experiments (Bullock et al., 2007). The positions of pressure transducers changed slightly during different phases of the experiments. Two arrangements of pressure transducers are presented here, i.e., z_1 for Case 1, 2 and 4; z_2 for Case 3 and 5. The total experimental force on the wall is calculated by the integral of the pressures along the wall from the vertical array of pressure transducers, and the numerical total force on the wall will be calculated in the same way. Wave pressures from the numerical simulations will be compared to the measured wave pressures at these specific elevations.

3.1. Mesh and time-step refinement studies

Case 4 is selected for the mesh and time-step refinement studies due to the large wave impacts and the complex wave surface profile with an air pocket. The refinement studies are conducted under four sets of meshes, as shown in Table 4. The number of cells per wavelength and per wave height is calculated based on the grid resolution at the slope. The overall and zoom-in view of M3 around the wall structure is shown in Fig. 5. The mesh is refined around the wall and the still water level. The time-step is controlled by the maximum Courant number, which varies from 0.5 to 0.3 for the converged mesh. Stream function theory is applied to generate regular waves with a ramp-up time (required duration to vary from 0 to the target value) of 4T. The time origin of the numerical results starts from the first wave impact after the initial wave reaches the wall. Several examples of the measured pressures can be found in Bredmose et al. (2009).

Wave impacts on a wall are highly-sensitive to variations in the free

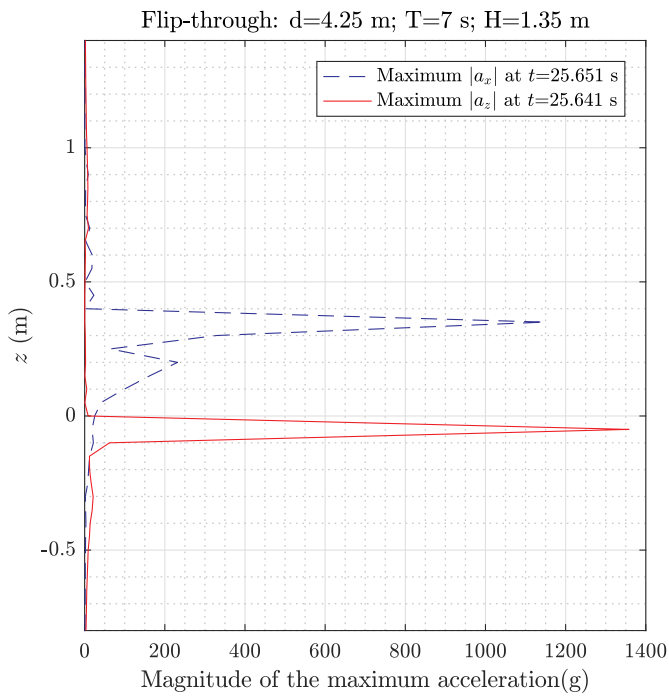

Fig. 18. Maximum magnitude of water acceleration on the wall along x and z axes during one wave period for Case 2: d = 4.25 m; T = 7 s; H = 1.35 m.

surface profiles (Peregrine, 2003; Bullock et al., 2007). Therefore, wave surface elevations for different grid resolutions are compared, and shown in Fig. 6. M1 underestimates the surface elevations compared to the other grid resolutions due to the larger numerical diffusion caused by the coarser mesh. The surface elevations for M2, M3 and M4 are similar to each other. The difference in the surface elevations between M3 and M4 is slightly smaller than that between M2 and M4, especially at the positions close to the wall. The relative variation is defined as the difference between the two results divided by the mean value of these two results. The maximum relative variation of the peak surface elevations between M3 and M4 is 3.6%. Therefore, M3 is considered to give sufficient numerical accuracy in the present study.

The time-step refinement study is conducted by decreasing the maximum Courant number from 0.5 to 0.3. The results of the time-step refinement are shown in Fig. 7. The relative variation of the surface elevations between these two Courant numbers is 4.5%. Therefore, the grid resolution of M3 with the maximum Courant number 0.5 is considered to give satisfactory numerical accuracy and will be used in the subsequent simulations. In addition, an extensive verification study on different cases based on the same numerical method can be found in Gatin (2018).

3.2. Characteristics of impact force and pressure under different breaking conditions

The free surface elevations, total impact force on the wall and the maximum pressure distribution are compared with the experimental measurements (Bullock et al., 2007) in this section. The total force (F_{Tot}) and the pressure ($p - p_0$) on the vertical wall is normalized by the $\rho g H^3$ and $\rho g H$, respectively; while the time has been normalized with $(H/g)^{1/2}$, where H is the incident wave height, p_0 is the atmospheric pressure. The impact force on the wall varies significantly every wave period even though the incident waves are regular (Bagnold, 1939). One important reason mentioned by Bullock et al. (2007) is due to the strong interaction of the reflected wave with incoming waves. The period with the first large impact on the wall is selected, which has the least disturbance from wave reflections.

3.2.1. Slightly-breaking wave impact

Slightly-breaking refers to the transitional conditions from non-breaking waves to fully developed wave impacts. The comparisons of the numerical and the experimental wave surface elevations for the slightly-breaking case are shown in Fig. 8. The surface elevations are plotted for one wave period at six different locations. The root mean square error (RMSE), denoted by E, is calculated with respect to the experimental surface elevations. The numerical surface elevations compare well with the experimental data generally. The predicted wave peaks agree with the measurements better when compared to the predicted wave troughs, especially at the location near the inlet. The RMSE of surface elevations is smallest at the nearest wave gauge to the wall, which is a positive indication for the wave force prediction.

Fig. 9 shows the comparison of the numerical and the experimental total forces on the vertical wall over one wave period. A zoom-in

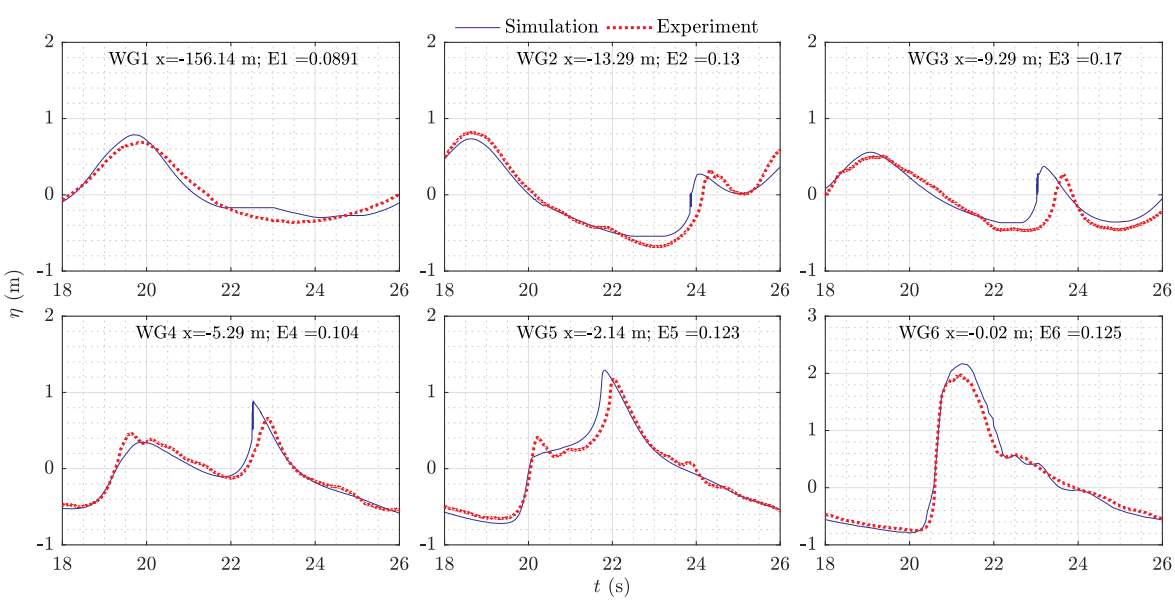

Fig. 19. Comparison of simulated and experimental surface elevations at different wave gauges for Case 3: d = 4.02 m; T = 8 s; H = 1.10 m.

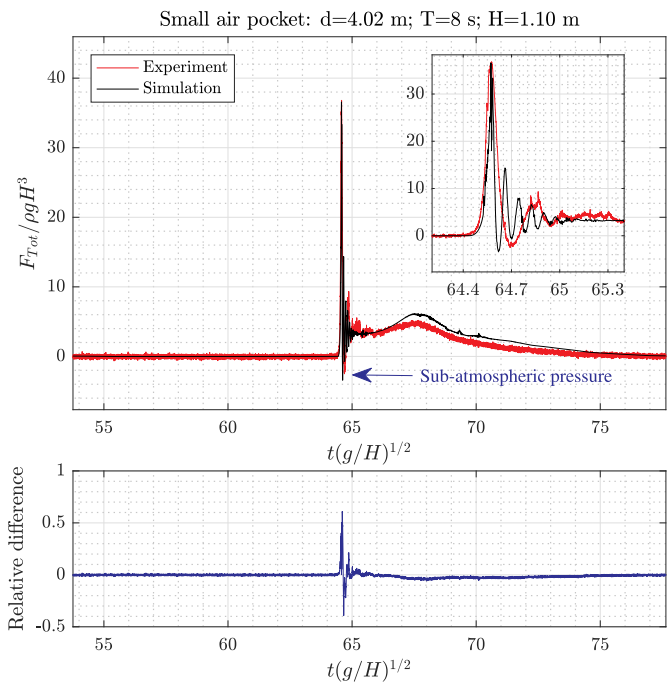

Fig. 20. Comparison of the simulated and experimental wave forces on the vertical wall for Case 3: d = 4.02 m; T = 8 s; H = 1.10 m, F_p = 36.57 (477.5 kN), t_I = 0.07 (24.3 ms).

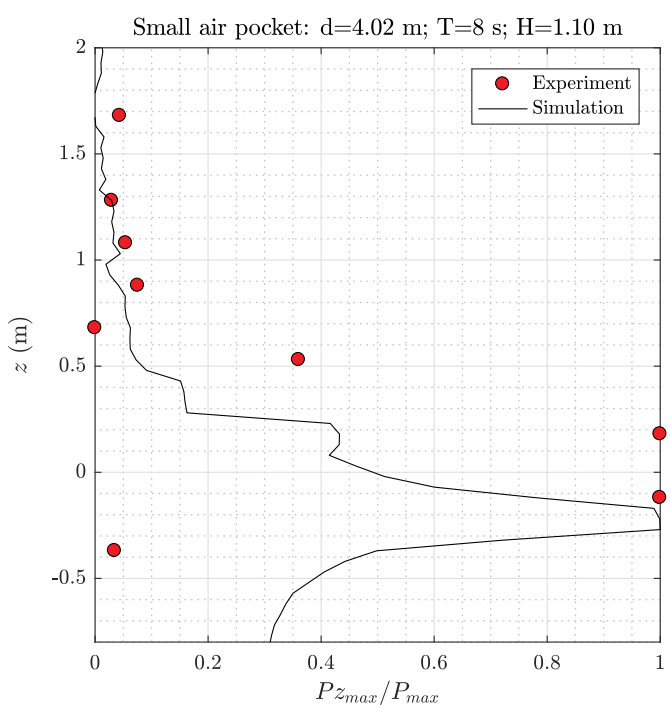

Fig. 21. Comparison of the simulated and experimental maximum pressures along the vertical wall for the breaking wave cases with a small air-pocket.

window around the peak value is presented at the top-right corner. The relative difference is shown in the lower figure of Fig. 9, which is defined as $(F_E - F_N)/\mathbf{max}(F_E)$, where F_E and F_N are the experimental and numerical total forces on the wall, respectively. A sharp spike in the total force is observed which is known as the impact force. There is a secondary bump after the main impact peak, which is the quasi-hydrostatic force. The maximum quasi-hydrostatic force, maximum total force F_p

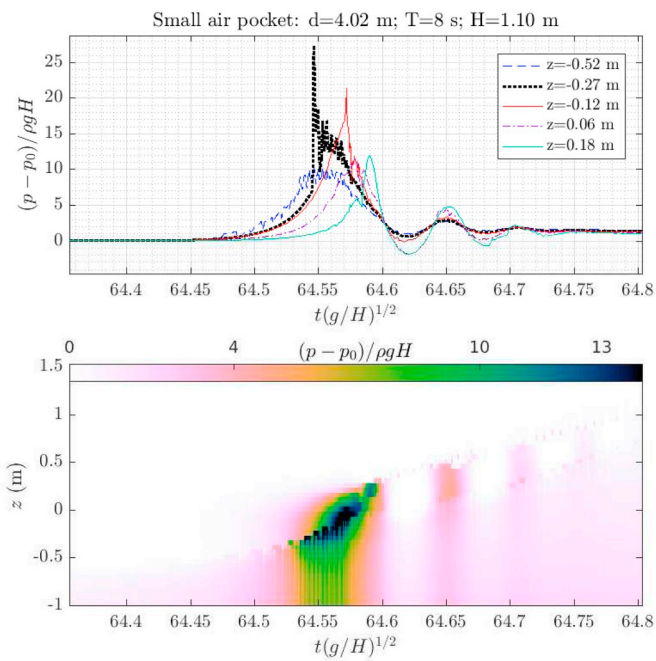

Fig. 22. Pressure variation and distribution along the vertical wall during an impact for Case 3: d = 4.02 m; T = 8 s; H = 1.10 m.

and impulse duration t_I of the impact force are indicated in Fig. 9. The peak impact force is 4.96 times the maximum quasi-hydrostatic force. This value is beyond the limits of the slightly-breaking given by Bullock et al. (2007), i.e., 1.0 to 2.5 times the maximum quasi-hydrostatic force. However, there are no clear boundaries between different impact types. The impact type is selected based on the slightly inclined surface profile as the wave impacts the vertical wall. The numerical total force agrees well with the experimental data in terms of quasi-hydrostatic force and the peak of the impact force. However, the duration of the impact force is underestimated when compared to the experimental total force. This is mainly due to the inconsistent pressure distribution along the wall between the simulation and the experiment, as shown in Fig. 10.

Fig. 10 shows the distributions of the maximum pressures along the wall from both the simulation and the experiment. The horizontal axis Pz_{max}/P_{max} is the ratio of maximum pressure at different vertical locations and the overall maximum pressure over one wave period. The vertical axis z indicates the vertical location. The general trend of the pressure distribution is well captured by the present numerical model, i.e., a sharp peak occurs just above still water level and then decreases rapidly on both sides. However, the position of the numerical P_{max} is around $z = 0.1$ m, which is lower than $z = 0.48$ m in the experiment. This means that the simulation has a slightly lower initial impact point than the experiment. The numerical pressures are almost zero when $z > 0.9$ m. However, the pressure is around $0.3P_{max}$ and nearly uniform along the wall when $z > 0.9$ m in the experiment. This discrepancy in pressure is due to that the different pressure gradients along the wall between the simulation and the experiment eventually result in the different wave run-up actions after the impact.

Rise time t_r is defined here as the time needed for the pressure signal to attain its maximum from the quasi-static pressure, and fall time t_f is defined as the time for the pressure signal reducing from the maximum to the quasi-static pressure. Fig. 11 shows the pressure variations during the impact at five locations and the pressure contour along the wall at different time instants. $p - p_0$ represent the pressure subtracted by the standard atmospheric pressure. The pressure signals at the lowest two transducers ($z = -0.60$ m, -0.35 m) are without impact characteristics. The initial impact point between the inclined wave front and the wall is between $z = -0.35$ m and $z = -0.05$ m. The peak pressure upon the

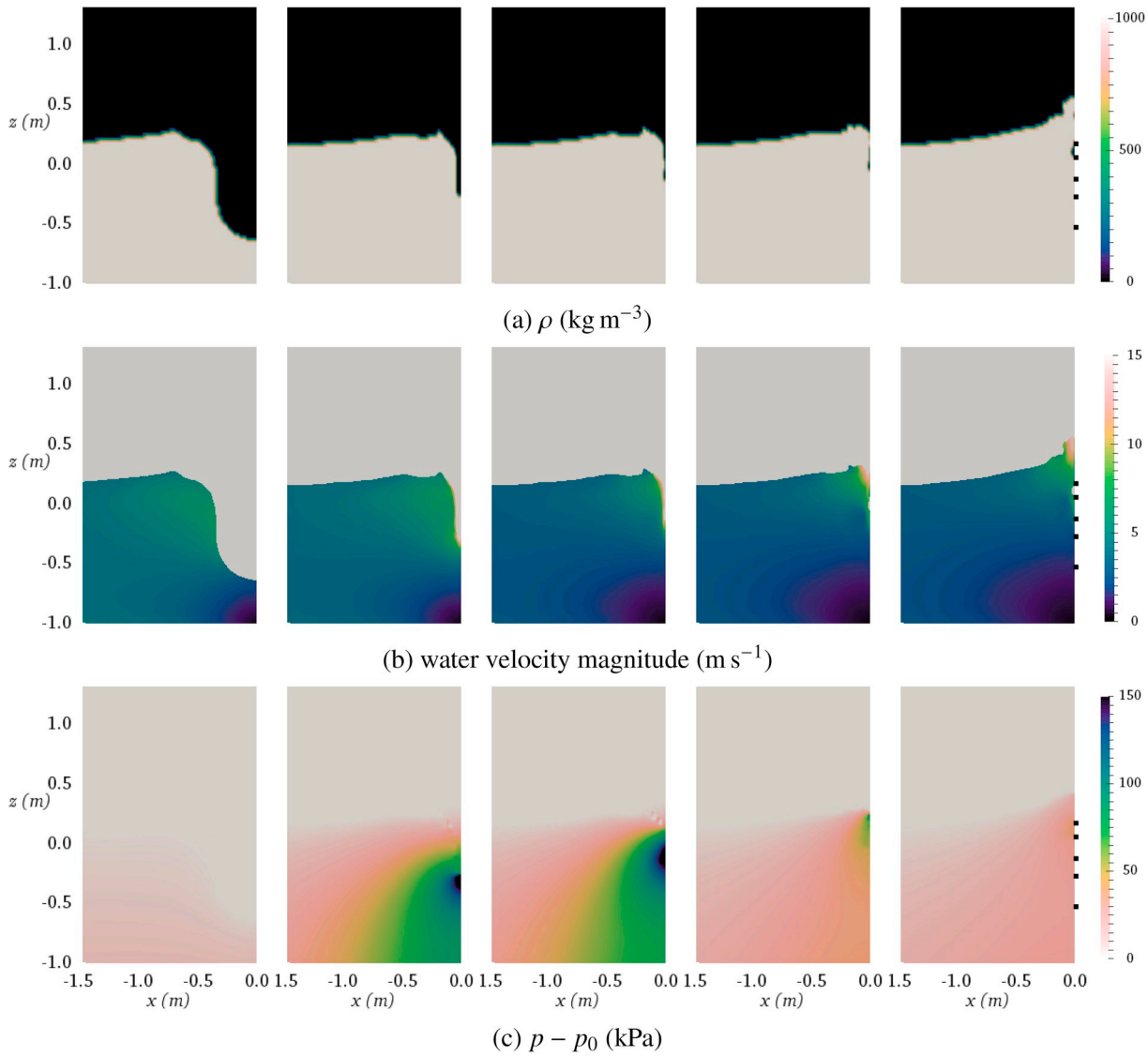

Fig. 23. Density, water velocity magnitude and pressure variations at different time instants during one impact for Case 3: d = 4.02 m; T = 8 s; H = 1.10 m, from left to right: $t_1 = 64.35$, $t_2 = 64.54$, $t_3 = 64.56$, $t_4 = 64.58$ and $t_5 = 64.65$.

initial impact point increases until $z = 0.10$ m and then decreases. The maximum pressure on the wall is around $15.47\rho gH$, which is characterized by a very short rise time and a slightly longer fall time. For the pressure variation at $z = 0.10$ m, the rise time is 1.9 ms and the fall time is 2.7 ms. There is a phase delay between different impact pressures due to the wave front moving up the wall. The pressure contour shows high pressure values distributed around the still water level while the pressure is almost uniform below $z = -0.5$ m.

Fig. 12 shows the density, water velocity magnitude and pressure variations at five time instants (from left to right): $t_1 = 38.57$, $t_2 = 38.65$, $t_3 = 38.68$, $t_4 = 38.70$ and $t_5 = 38.73$. Time instants t_3, t_4 and t_5 are the time instants that correspond to the peak pressures at $z = -0.05$ m, 0.10 m and 0.35 m. Five locations presented in Fig. 11 are indicated by five black points on the wall. A sharp interface between the water phase and the air phase is captured in the density field, as shown in Fig. 12a. The characteristic of the slightly-breaking impact is clearly shown in Fig. 12a and 12b at time t_1, i.e., the wave hits the wall with a slightly inclined surface. The pressure around the wall is low at t_1 before the impact. The wave front with a large velocity acts on the wall at around $z = -0.15$ m from time instant t_2. The largeest pressure on the wall is observed where the water velocity is highest. The contact point with the large water velocity then travels up along the wall to $z = -0.05$ m; 0.10 m and 0.35 m at t_3, t_4 and t_5, respectively. The pressures at these three locations reach their peak values rapidly with the large velocity reducing to zero on the wall. The maximum pressure on the wall occurs at t_3, which also corresponds to the time of the peak total force in Fig. 9. During the impact pulse, the pressure is largest at the impact point and decreases downward along the wall within a diameter of approximately $0.27d_w$ (d_w is the water depth at wall).

3.2.2. Flip-through wave impact

The wave for the flip-through case is more developed when compared to the slightly-breaking case, and approaches the wall with a nearly vertical front face instead of an inclined face. Fig. 13 shows the comparisons of the numerical and the experimental wave surface elevations at six wave gauges for Case 2. The numerical surface elevations generally agree well with the experiments at different locations. The numerical maximum surface elevation at WG6 is slightly higher than the experimental data.

Fig. 14 presents the comparison of the numerical and the experimental total forces on the vertical wall over one wave period for Case 2. The zoom-in window at the top-right corner shows a very good agreement between the numerical and experimental impact forces. The peak value, variation tendency, rise time and fall time of the impact are well

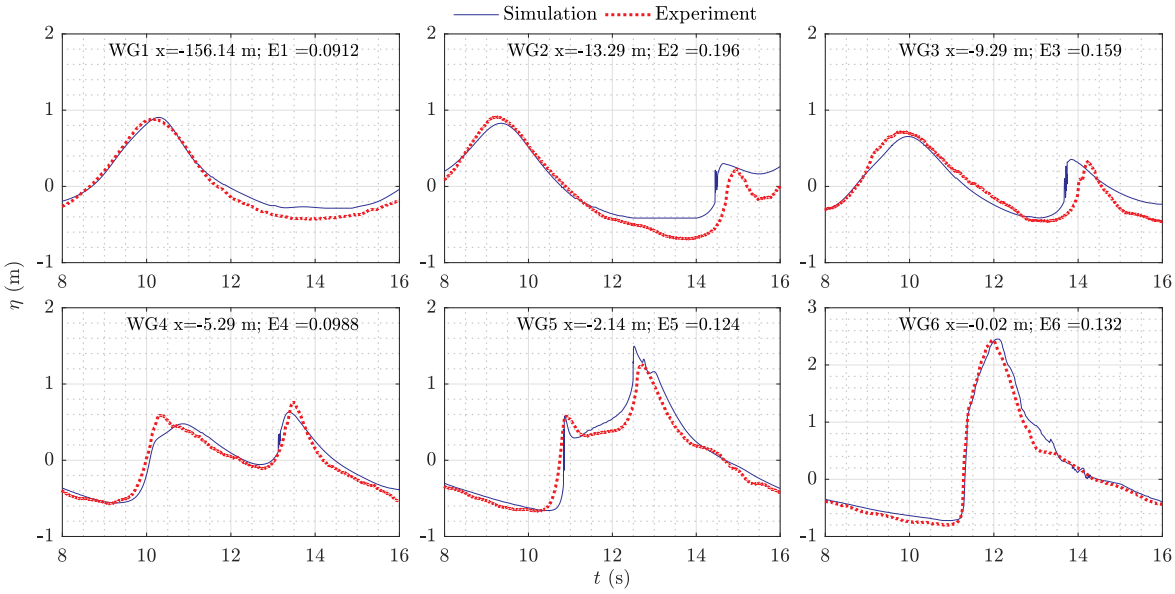

Fig. 24. Comparison of simulated and experimental surface elevations at different wave gauges for Case 4: d = 4.00 m; T = 8 s; H = 1.25 m.

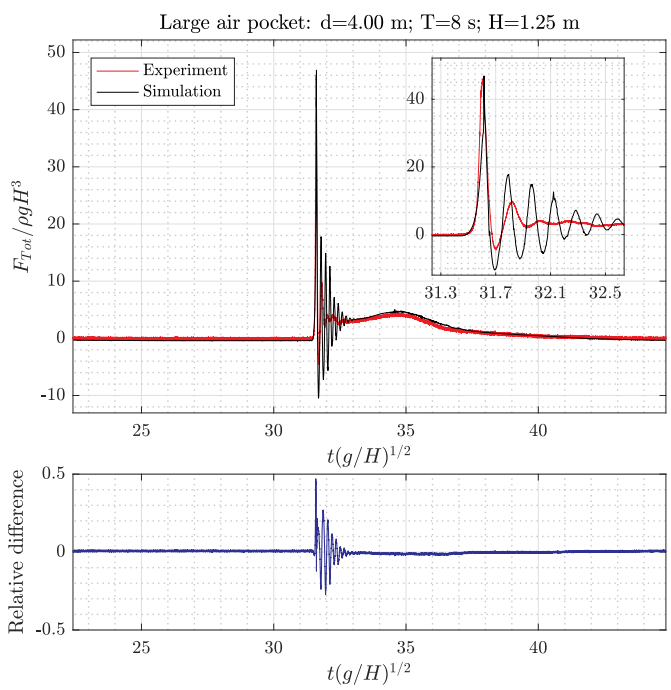

Fig. 25. Comparison of the simulated and experimental wave forces on the vertical wall for Case 4: d = 4.00 m; T = 8 s; H = 1.25 m, $F_p = 46.91$ (898.8 kN), $t_I = 0.08$ (29.5 ms).

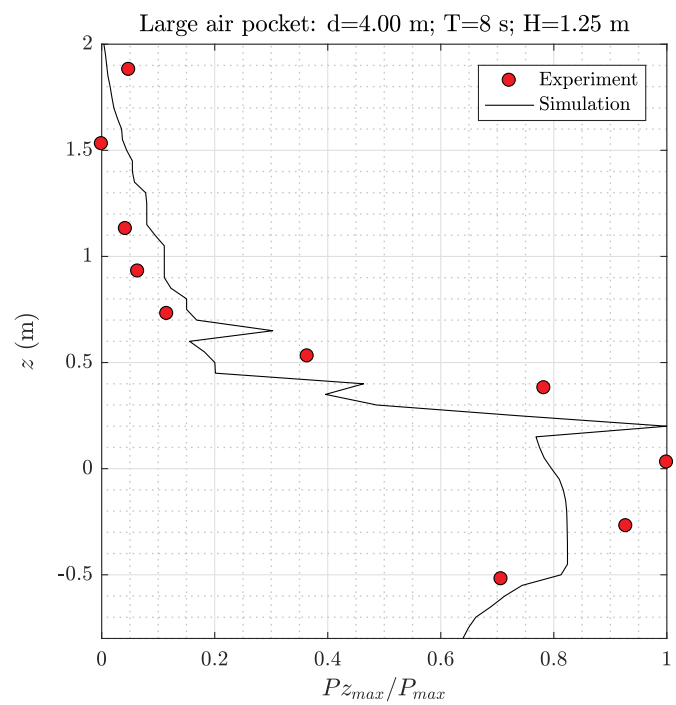

Fig. 26. Comparison of the simulated and experimental maximum pressures along the vertical wall for the breaking wave cases with a large air-pocket.

captured in the numerical simulation. A much sharper spike of the flip-through total force with a larger peak value and a shorter duration can be seen in Fig. 14 when compared to the slightly-breaking total force. The ratio of the maximum total force and the maximum quasi-hydrostatic force is 11 for the flip-through case, which is more than twice of that for the slightly-breaking case. Both the numerical and the experimental maximum pressure (Pz_{max}) distributions along the wall are shown in Fig. 15. The peak of the numerical Pz_{max} occurs at $z = 0.25$ m, which is close to $z = 0.28$ m as measured in the experiment. The distribution of Pz_{max} of the flip-through case is more localized in space than the slightly-breaking case, shown as a sharper variation of Pz_{max} in Fig. 15. The numerical Pz_{max} decreases rapidly from P_{max} to nearly zero in the range of $z = 0.25$ m to $z = 0.70$ m. In the range of $z = 0.25$ m to $z = -0.68$ m, the numerical Pz_{max} decreases from the P_{max} to $0.18P_{max}$ and then remains constant when $z = -0.68$ m. The experimental data have similar vertical spatial variations.

The pressure variations during the impact at the five elevations and the pressure contour along the wall at different time instants are shown in Fig. 16. Similar to the slightly-breaking case, the pressures at $z = -0.50$ m, -0.10 m are non-impulsive. The initial impact point is between $z = -0.10$ m and 0.10 m. The largest pressure occurs at $z = 0.25$ m with a value of $38.31\rho gH$ (507.3 kPa), i.e., around $9.23\rho g(d +$

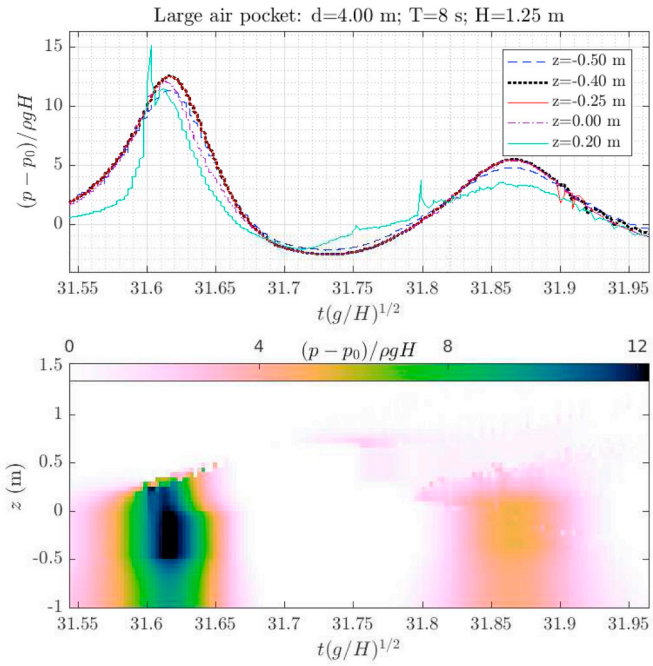

Fig. 27. Pressure variation and distribution along the vertical wall during an impact for Case 4: d = 4.00 m; T = 8 s; H = 1.25 m.

H), which is close to $10\rho g(d+H)$ as mentioned by Peregrine (2003). The rise time of the pressure at $z = 0.25$ m is 0.3 ms, which is around $1/6t_r$ of the slightly-breaking case. The corresponding fall time is 1.0 ms which is around $1/3t_f$ of the slightly-breaking case. The peak pressure at $z = 0.25$ m is much larger than that at the surrounding elevations, which shows that the impact is localized in space and time as expected for a flip-through type impact.

Fig. 17 shows the density, water velocity magnitude and pressure variations for the flip-through case at five time instants (from left to right): $t_1 = 69.07$, $t_2 = 69.13$, $t_3 = 69.14$, $t_4 = 69.16$ and $t_5 = 69.18$. Time instants t_3 to t_5 correspond to the peak pressures at $z = 0.10$ m, 0.25 m and 0.45 m, respectively. The density field at t_1 presents a nearly vertical front face which is paralleled to the wall. However, this wave front is not a fully vertical wave front. There is a small region of the wave front with an inclined surface. This impact has the typical flip-through characteristics. However, the impact value is not as large as that we could expect for a perfect flip-through case (Obhrai et al., 2005). The initial impact on the wall is considered to occur at t_2 with a large velocity occurring as the wave front hits the wall. The contact point rises up the wall with a maximum pressure on the wall increasing until t_4 and then decreasing.

Another typical feature of the flip-through case is the large water acceleration at the wall, which is over 1000g reported by Peregrine (2003) and up to 1500g measured by Lugni et al. (2006). The maximum acceleration magnitudes over one wave period at the wall along x and z axes are plotted against the vertical location in Fig. 18. In the present simulation, the largest vertical acceleration ($|a_z|$) is 1358g, which occurs at the location of $z = -0.05$ m and at time instant t_2. The largest horizontal acceleration ($|a_x|$) is 1147g, which occurs at the location of $z = -0.35$ m and at time instant t_4. This illustrates the process of the flip-through impact. Firstly, the largest $|a_z|$ occurs together with the initial impact (t_2). This large $|a_z|$ accelerates the water along the wall and generates the vertical jet. Then the largest $|a_x|$ occurs together with the largest pressure (t_4) on the wall. The largest pressure on the wall is generated by the change of the water's momentum, i.e., the large horizontal velocity at the wave front reduces to zero on the wall in a short time.

3.2.3. Wave impact with air pocket

(a) *Wave impact with a small air pocket*

The vertical wave front can further develop to a slightly overturned wave front and trap a small air pocket at the wave crest. Fig. 19 shows the comparisons of the numerical and the experimental wave surface elevations at six wave gauges for Case 3. The numerical surface elevations agree well with the experiment al data at six wave gauges. However, the peak surface elevations are slightly over-estimated in the simulations.

Fig. 20 shows the comparison of the numerical and the experimental total forces on the vertical wall over one wave period for Case 3. The comparison in the zoom-in window at the top-right corner shows a good agreement between the numerical and experimental impact forces in terms of the peak values and rise times. However, the fall time of the impact is slightly underestimated in the numerical simulation. The maximum total force is around 6.06 times the maximum quasi-hydrostatic force. The negative sub-atmospheric pressure due to the decompression of the trapped air pocket is well captured, which shows a similar value with the experimental data shown in Fig. 20. The total force oscillates for several cycles after the sub-atmospheric pressure, and is damped to the quasi-hydrostatic force gradually. The numerical simulations predict a larger frequency and amplitude of the oscillations when compared to the experiment, which reveals that the behaviour of the air pocket is not identical in the simulation and the experiment. The numerical quasi-hydrostatic force is slightly larger than the experiment due to the higher peak surface elevations predicted in the simulation (see also Fig. 19).

Fig. 21 shows the numerical and experimental maximum pressure distributions along the wall for Case 3. The peak of the numerical Pz_{max} occurs at $z = -0.27$ m and remains almost constant until $z = -0.17$ m. In the experiment, this constant Pz_{max} region is from $z = -0.12$ m to $z = 0.18$ m, which has a higher location and wider range than the simulation. A secondary peak is observed at $z = 0.18$ m in the simulation and is supposed to be related to the trapped air pocket. The Pz_{max} declines sharply from both sides of the maximum pressure and is close to zero when $z >= 0.70$ m, which indicates a thin water jet here and is similar to the flip-through impact.

Fig. 22 shows the pressure variations and air entrapment during the impact at five locations and the pressure contour along the wall at different time instants for Case 3. The pressure at $z = -0.52$ m is without impact effects. The largest pressure occurs at $z = 0.27$ m with a value of $27.34\rho gH$ (295 kPa). Similar to flip-through impact, the pressure at $z = 0.27$ m has very short rise and fall times, i.e., $t_r = 0.4$ ms and $t_f = 0.5$ ms. The behaviour of the pressure varies drastically from $z = 0.27$ m to the secondary peak (see Fig. 21) at $z = 0.18$ m. The peak pressure reduces to $11.89\rho gH$ (128.3 kPa) which is less than half of the maximum pressure (at $z = 0.27$ m). The rise and fall times t_r and t_f increase to 3.3 ms and 3.5 ms, respectively, which are around 8 times larger than the t_r and t_f at $z = 0.27$ m. The negative sub-atmospheric pressures are observed at $z = 0.06$ m and 0.18 m with damped oscillations, which indicates these two locations are within the air pocket region. The pressure contour in Fig. 22 shows that the pressure is first localized in a small area, then starts to spread within a small range when the air pocket is trapped. The pressure oscillations are also clearly shown in the pressure contour in Fig. 22 after the entrapment of the air pocket.

Fig. 23 shows the density, water velocity magnitude and pressure variations for Case 3 at five time instants (from left to right): $t_1 = 64.35$, $t_2 = 64.54$, $t_3 = 64.56$, $t_4 = 64.58$ and $t_5 = 64.65$. Time instants t_2 to t_4 are the time instants of the peak pressures at $z = -0.27$ m, -0.12 m and 0.18 m, respectively, whereas t_5 is the time instant of the second peak in the pressure at $z = 0.18$ m. A vertical wave front is observed in front of the wall at t_1. The maximum impact pressure occurs at t_2 with a large velocity acting at $z = -0.27$ m on the wall. The pressure distributions

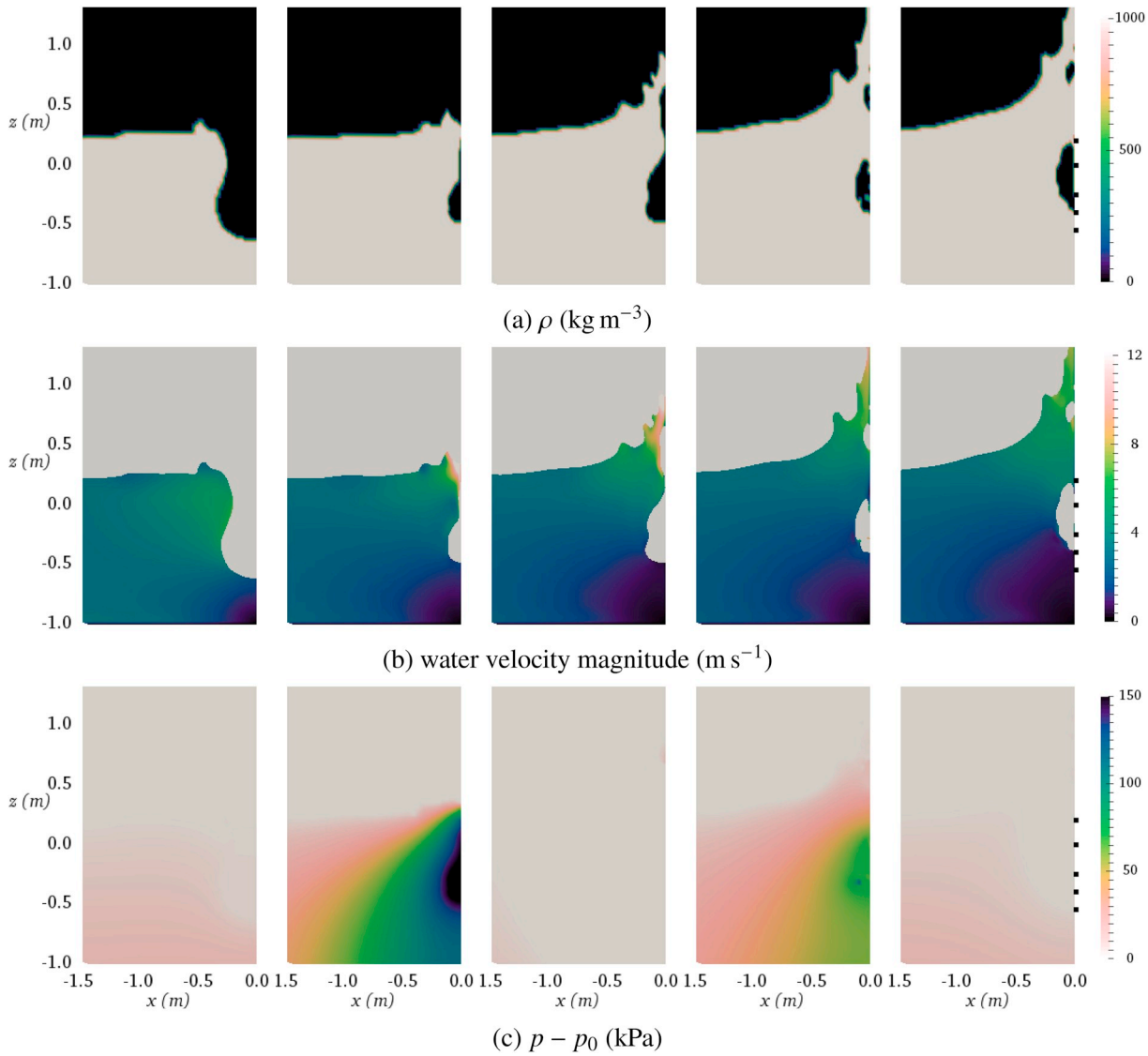

Fig. 28. Density, water velocity magnitude and pressure variations at different time instants during one impact for Case 4: d = 4.00 m; T = 8 s; H = 1.25 m.

before the trapped air pocket are similar with the flip-through impact, i.e., largest pressure is focused around the impact point. A very small air pocket is trapped at t_3 and travels up along the wall with the wave run-up, as shown in the density field of Fig. 23. The largest pressure occurs within the air pocket region at around the time t_3. However, the compression and expansion of the air pocket are not observed clearly due to the small size of the air pocket.

(b) Wave impact with a large air pocket

A large air pocket is obtained with a larger incident wave height, while the water depth and wave period are similar to the small air pocket case (H increases from 1.10 m to 1.25 m). The wave front overturns apparently before reaching the wall, and the breaker tongue hits the wall and traps an air pocket. Fig. 24 shows the comparison between the present simulated and the experimental surface elevations at six wave gauges for Case 4. The numerical surface elevations agree well with that of the experiments at all the wave gauges. The surface peak is slightly overestimated at WG6, which can result in a higher quasi-hydrostatic force in the simulation.

Fig. 25 shows the comparison of the numerical and the experimental total forces on the vertical wall over one wave period for Case 4. The zoom-in window shows that the simulation results have a good agreement with the experimental data in terms of the peak value, rise and fall times of the impact. The maximum total force is around 9.93 times the maximum quasi-hydrostatic force. The amplitude, frequency and duration of the oscillations after the main impact are over-predicted in the simulation. The numerical maximum oscillation amplitude is $27.23\rho gH^3$ (521.8 kN), which is around two times larger than that in the experiment and also two times larger than that of the small air pocket case. Therefore, the behaviour of the oscillations can be related to the size of the air pocket in the simulation.

Fig. 26 compares the distributions of the numerical and experimental Pz_{max} along the wall, and a good agreement is achieved between the two sets of results. A sharp peak occurs with a maximum value of Pz_{max} at $z = 0.20$ m in the simulation. A nearly uniform Pz_{max} distribution just below this peak point is observed between $z = -0.50$ m and $z = 0.15$ m, with a value of around 80% of P_{max}.

Fig. 27 presents the pressure variations while entrapping the air pocket at five locations and the pressure contour along the wall at different time instants for Case 4. The pronounced differences of the pressure variations are observed for the case with a large air pocket as compared to the other impact types. The pressures from $z = -0.50$ m–0.00 m are characterized by almost identical variations in

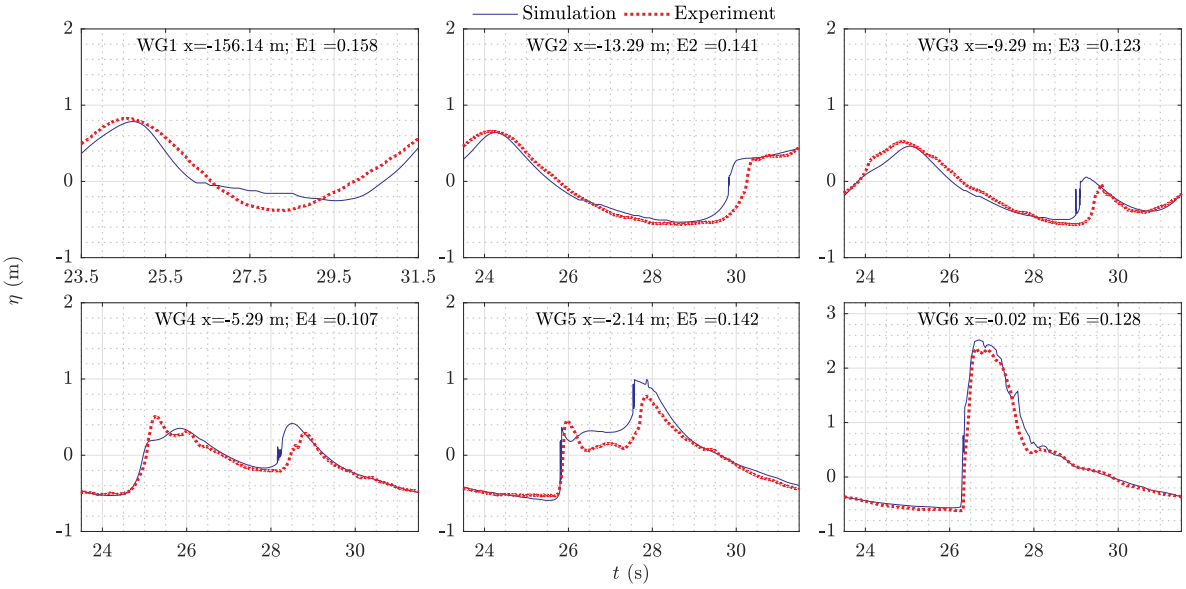

Fig. 29. Comparison of simulated and experimental surface elevations at different wave gauges for Case 5: d = 3.70 m; T = 8 s; H = 1.00 m.

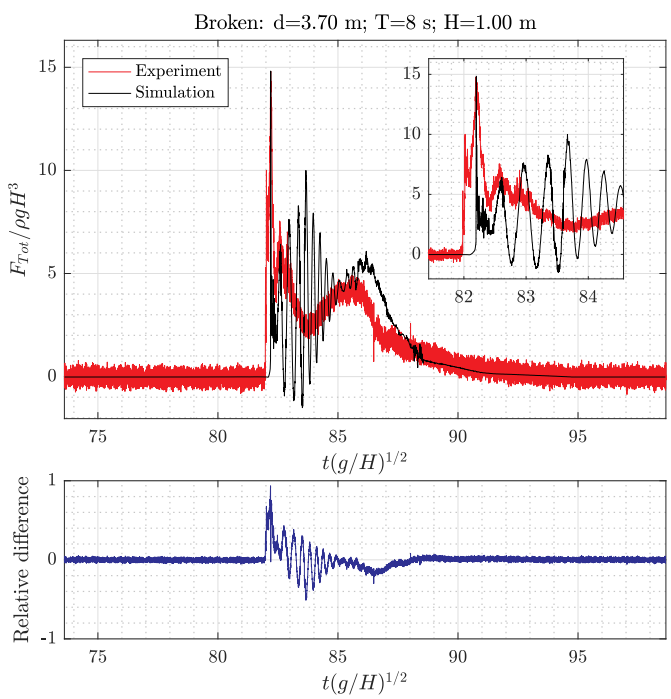

Fig. 30. Comparison of the simulated and experimental wave forces on the vertical wall for Case 5: d = 3.70 m; T = 8 s; H = 1.00 m, F_p = 14.82 (145.4 kN), t_I = 0.03 (9.1 ms).

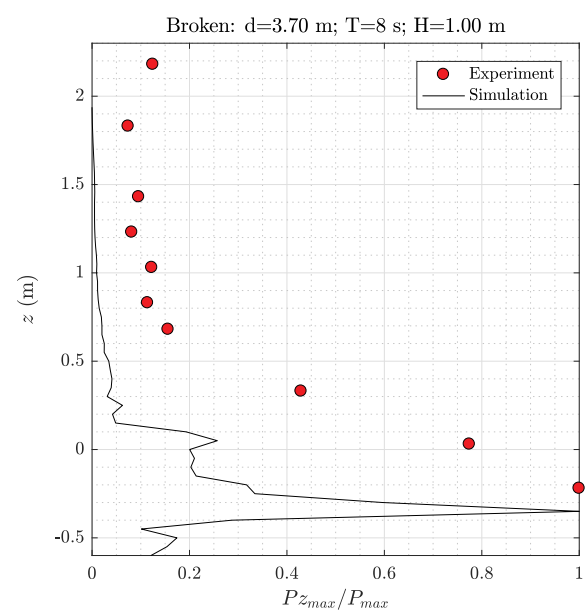

Fig. 31. Comparison of the simulated and experimental maximum pressures along the vertical wall for the broken wave case.

damped sinusoidal signals. The peaks and phases within this region are similar to each other. They are inside the region of nearly uniform Pz_{max} shown in Fig. 26, which correspond to the trapped air pocket area. The rise time and fall time are t_r = 49.0 ms and t_f = 41.8 ms, respectively, which are approximately 100 times longer than that in the flip-through case. The peak pressure is around 12.22 ρgH, i.e., 150 kPa, which is less than $1/3P_{max}$ of the flip-through case. The pressure at z = 0.20 m (maximum pressure) is a combination of an impact with a short rise time and a damped sinusoidal variation induced by the trapped air pocket, which indicates that the breaker tongue hits this point first, forms a sharp impact and then oscillates due to the cushioning effects of the entrapped air pocket. The cushioning effects are also indicated by the banded pressure contour in Fig. 27. The maximum pressure is imposed uniformly over the air pocket region, and decreases at the other locations.

Fig. 28 shows the density, water velocity magnitude and pressure variations for Case 4 at five time instants (from left to right): t_1 = 31.45, t_2 = 31.61, t_3 = 31.72, t_4 = 31.86 and t_5 = 31.95. Time instants t_2 and t_4 correspond to the first and second peaks of the oscillating pressures, t_3 is the time instant of the first trough of the pressures. The overturned wave front is observed at t_1 when the formed breaker tongue is approaching the wall. The impact peak occurs at around t_2 when the wave front with the largest water velocity hits the wall at z = 0.20 m, as shown in the velocity field in Fig. 28, which results in the sharp peak pressures in

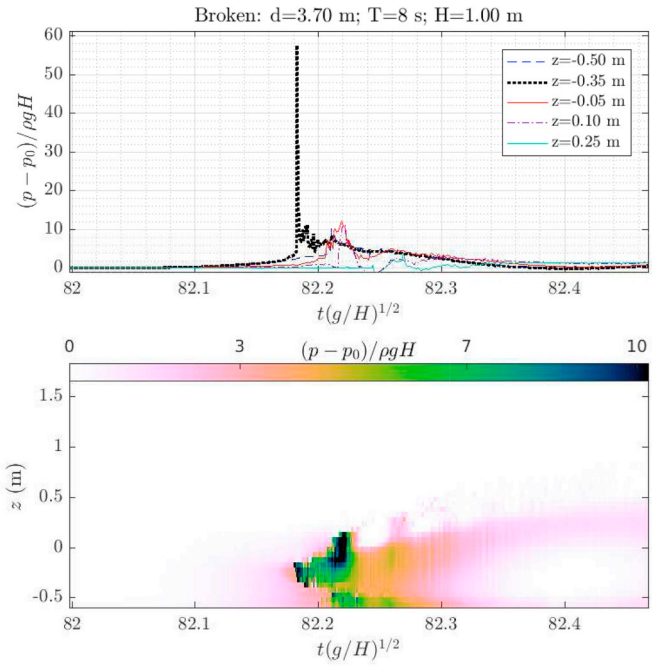

Fig. 32. Pressure variation and distribution along the vertical wall during an impact for Case 5: d = 3.70 m; T = 8 s; H = 1.00 m.

Figs. 26 and 27. The air pocket is enclosed and initially compressed after t_2. The compression and expansion of the air pocket is clearly shown in the density field. The size of the air pocket, especially the vertical size, increases from t_2 to t_3, decreases from t_3 to t_4, and increases again from t_4 to t_5. The corresponding pressures show that the expansion of the air pocket at t_3 generates the pressure trough, which is the sub-atmospheric pressure in Fig. 25. The pressure reaches a second peak with a lower value when the air pocket is compressed again at t_4, and reduces again with the air pocket expansion. The alternating compression and expansion of the air pocket produce the damped oscillations of the pressure, which is consistent with the observations reported by Bullock et al. (2007).

As a summary, the most distinctive features for the impact with an air pocket are the negative sub-atmospheric pressure and the damped oscillations. These features can be recognized in the force or pressure variations easily. As compared to the slightly-breaking and the flip-through impact types, the duration of the maximum pressure within the air pocket is much longer, which is up to 100 times longer. However, the peak pressure is reduced by the air pocket. The pressure distribution in the air pocket region is almost uniform. On the contrary, the flip-through impact has the largest pressure focused on a small area, and this area can be infinitely small in theory. Therefore, in the context of practical engineering, the flip-through impact tends to generate local damage of the structure with the very large pressures that are localized in space and time. On the other hand, the impact with a large air pocket can inflict global damage of the structure due to the long impulse duration and large action area. In addition, the pressure oscillations could possibly excite the higher-order vibrations for some structures, resulting in more damage. Therefore, both types are considered important extreme conditions for the design of coastal structures.

3.2.4. Broken wave impact

According to Svendsen et al. (1978), the surf zone after the breaking point can be divided into three regions based on the development of the broken wave, i.e., 1) the outer region with a rapid change in wave shape; 2) the inner region with a slow change in wave shape; 3) the run-up region without a surface roller. Therefore, the broken wave-wall interaction can have various scenarios depending on which region the wall is located in. In the broken wave impact example given here, the breaker hits the wall in the outer region at the time instant when the wave front curls over, plunges into the lower wave surface and forms an air pocket. The comparisons of the numerical and experimental surface elevations at six wave gauges for Case 5 are shown in Fig. 29. The numerical results agree well with the experimental data, especially for the wave gauges on the slopes and close to the vertical wall.

Fig. 30 shows the comparison of the numerical and the experimental total forces on the vertical wall over one wave period for Case 5. The peak total force is 145.4 kN, i.e., around 3 times the maximum quasi-hydrostatic force, which is much lower compared to the other cases. The peak value of the total force is well captured in the simulation as compared to the experiment. However, some discrepancies can be seen in the simulation, i.e., the impact duration is underestimated dramatically, the oscillations and the quasi-hydrostatic force are overestimated. This is mainly due to the insufficient experimental data obtained from the pressure transducers in this case. The water depth of Case 5 is smaller than the other cases, and there is only one of ten pressure transducers under the still water level. The maximum pressure usually occurs around the still water level according to the study by Bullock et al. (2007). Therefore, the integral of the pressure is highly sensitive to the only pressure transducer under the still water level, and a small difference in the pressure distribution can cause a large difference in the total force. The numerical and experimental pressure distributions along the wall are shown in Fig. 31. The general trends of the pressure variations along the wall are similar in the simulations and the experiments, i.e., the maximum Pz_{max} occurs under the still water level, decreases rapidly up along the wall, and stabilizes at a small value at the higher locations of the wall. The numerical P_{max} is at $z = -0.35$ m, which is slightly lower than $z = -0.22$ m in the experiment.

Fig. 32 shows the pressure variations during the impact at five locations and the pressure contour along the wall at different time instants for Case 5. The pressure at $z = -0.50$ m is a typical impact pressure with a rise time of 0.2 ms, a fall time of 0.6 ms and a peak value of $56.4\rho gH$ (around 563.8 kPa). This peak value is even larger than the peak flip-through pressure, although the total force is around 8 times smaller than the flip-through case. The peak pressures at the other locations are much smaller than that at $z = -0.35$ m. The pressure contour shows that the initial impact occurs at around $t(g/H)^{1/2} = 82.18$ ($t = 26.24\ s$), and another peak in pressure occurs at around $t(g/H)^{1/2} = 82.22$ ($t = 26.25\ s$).

Fig. 33 shows the density, water velocity magnitude and pressure variations for the Case 5 at five time instants (from left to right): $t_1 = 82.00$, $t_2 = 82.15$, $t_3 = 82.18$, $t_4 = 82.22$ and $t_5 = 82.25$. Time instants t_3 and t_4 correspond to the pressure peaks at $z = -0.35$ m and -0.05 m. The density and velocity fields at t_1 and t_2 show the formation of the water jet with the development of the overturning wave crest after the breaking point. The water jet moves forward to approach the wall and also downwards to form an air pocket. Right before the closure of the air pocket, the water jet with high velocity hits the wall at t_3. Therefore, the large impact pressure is observed at $z = -0.35$ m at the same time, which is also shown in the pressure field. Then the water moves from the high-pressure to the low-pressure regions at both sides and encloses the air pocket rapidly at t_4. The large pressure region spreads with a diameter of 0.3 m around the still water level, and last for around 2.4 ms as shown in Fig. 32. The compression and expansion of the air pocket results in the extra oscillations after the main peak in Fig. 30.

3.3. Discussion

In general, the numerical results are in good agreement with the experimental data for four different types of wave impacts in terms of the total forces and pressure distributions on the wall. However, some discrepancies are observed between the simulations and the experiments

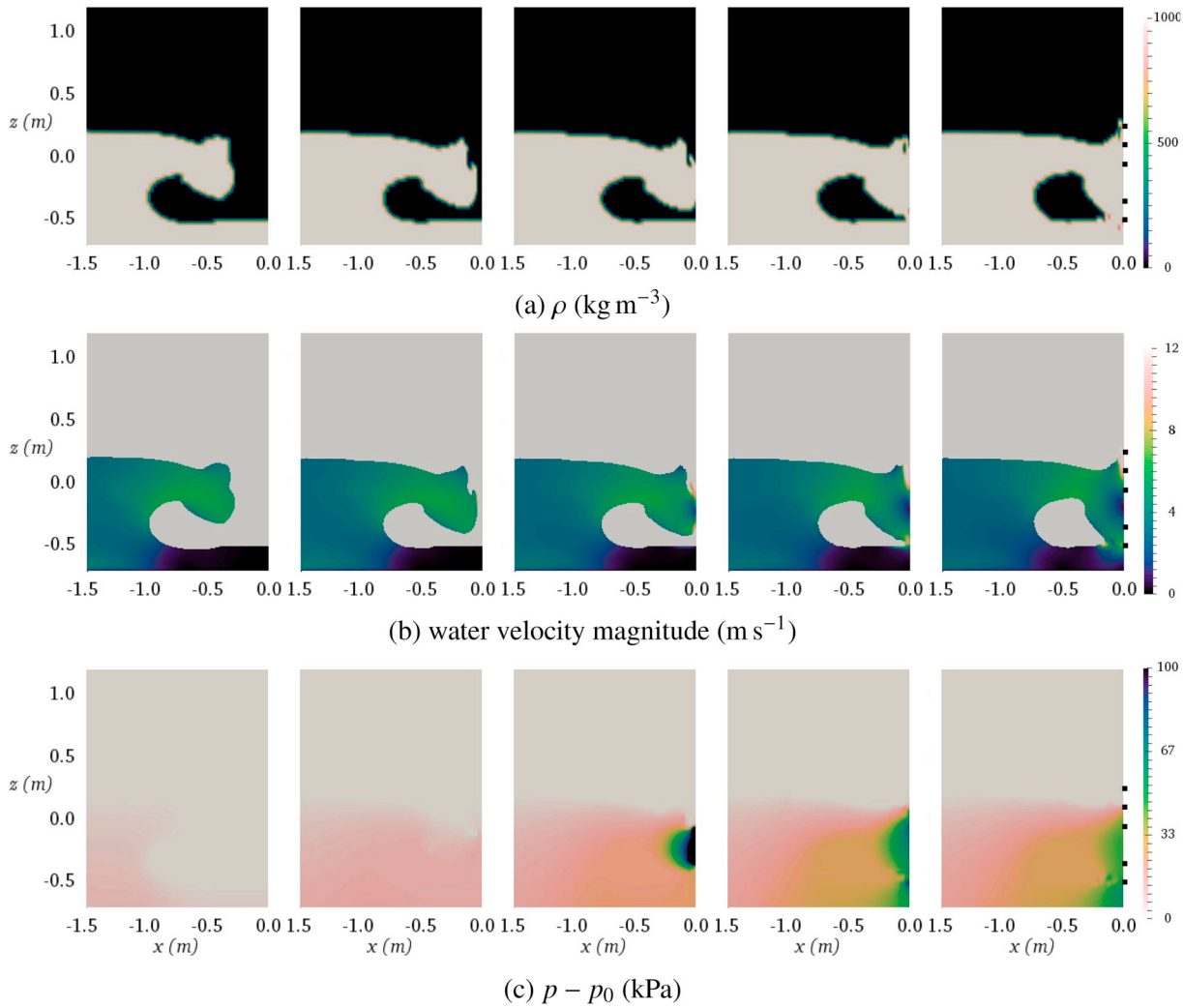

Fig. 33. Density, water velocity magnitude and pressure variations at different time instants during one impact for Case 5: d = 3.70 m; T = 8 s; H = 1.00 m, from left to right: $t_1 = 82.00$, $t_2 = 82.15$, $t_3 = 82.18$, $t_4 = 82.22$ and $t_5 = 82.25$.

and are discussed in this section.

(i) The first wave gauge WG1 is located 81.15 m away from the velocity inlet. The numerical surface elevations at WG1 always show a shallower and flatter wave trough than in the experiments. The agreement between the simulations and the experiments is improved as the waves propagate up the slope and towards the vertical wall. The most likely reason is that the input waves from the inlet are not identical in the simulations and the experiments. The nonlinear stream function wave theory is used in the simulation according to Le Méhauté (2013) who classified the wave shapes based on the water depth, the wave height and the wave period. The experimental wave input appears to be a deep water wave that develops into a shallow water wave as it propagates over the ramp. However, the experimental wave input signal is not documented or presented in any published papers. Therefore, the stream-function wave is used in the present simulations.

(ii) The wave absorption capacities at the inlet of the present simulations are different from that of the experiments. In the numerical simulations, the relaxation method is used in the inlet relaxation zone to generate the regular waves and absorb the reflected waves from the vertical wall. In theory, the reflected waves can be absorbed completely and a clean wave input can be given at the end of the wave generation zone. In the GWK experiments, the wavemaker is also equipped with an active wave absorption system to avoid unwanted reflections of waves. However, the experimental absorption rate is not 100% effective and is around 95% in practice. This could result in the differences in wave shapes between the experiments and the simulations.

(iii) The number of pressure transducers in the experiment are limited. The total force is calculated based on the integral of the pressures from the 10 transducers along the wall. The integral can represent the total force reasonably, provided that the pressure transducers have covered the whole impact region. However, for the broken wave case, only one pressure transducer is located in the large pressure region, which is not sufficient to calculate the total impact force on the wall.

(iv) There are three impact cases involving the compressible air pocket in the present study, i.e., the small air pocket case, the large air pocket case and the broken wave case. The compressibility of the trapped air pocket is captured in the numerical simulation, shown as the pressure oscillations after the main peak. However, the common problem of the numerical results for these cases is overestimating the magnitude and the frequency of the pressure oscillations as compared to the experiment. The main reason for this is that the air escape in the experiment is not properly simulated in the present numerical model. As summarized by Peregrine (2003), the air pocket can break up into small bubbles rapidly under a violent wave impact. Fig. 34 shows a

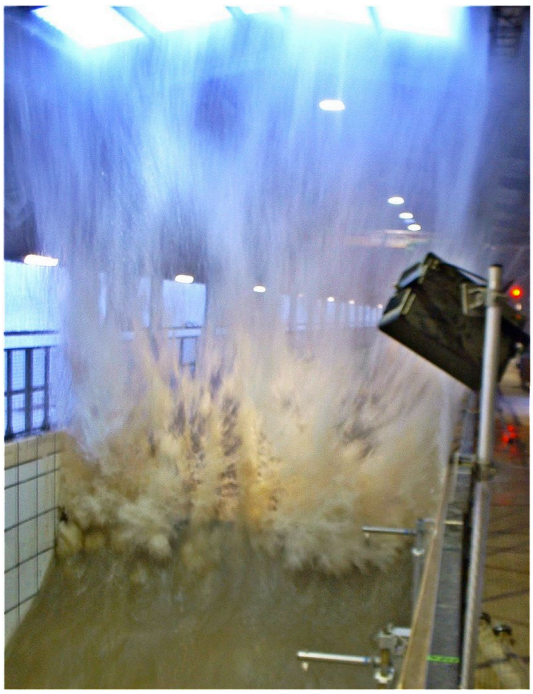

Fig. 34. Air escape from the trapped air pocket in the experiment.

Fig. 35. The model walls with holes in the experiment.

picture of one impact with a trapped air pocket in the experiment, which indicates clearly that the air pocket breaks up into small air bubbles and the air explodes out of the back of the wave due to the high pressure. However, dispersed air bubbles are not considered in the present numerical simulation.

In addition, the physical model wall is not completely solid, as shown in Fig. 35. The experimental wall model has 18 small holes where air and water can go through during the impact. Therefore, the air can escape through the holes in the air pocket case. The numerical simulations do not include the holes due to the present two-dimensional simulations. In summary, the numerical model overestimates the pressure oscillations after the main peak due to the inaccurate capture of the air escape during impacts with an air pocket.

4. Conclusions

A two-dimensional two-phase CFD model with incompressible water and compressible air has been used to simulate breaking wave impacts on a vertical wall. The Ghost Fluid Method is used to consider the sharp change in fluid properties and the jump in compressibility across the free surface. Four different types of breaking wave impacts on the vertical wall have been simulated. The numerical results are compared with the experimental data in terms of the surface elevations, the pressure distributions, and the total force on the wall. Generally, good agreements are obtained between the simulations and the experiments for all the impact types. The characteristics of different breaking wave impacts captured in the simulation are summarized as follows:

(i) For the slightly-breaking impact, the maximum total force is 4.96 times the maximum quasi-hydrostatic force. The maximum pressure on the wall occurs at $z = 0.10$ m with a value of $15.47\rho gH$, which is characterized by a very short rise time 1.9 ms and a slightly longer fall time 2.7 ms. The pressure is largest at the impact point and decreases down along the wall within a diameter of approximately 0.27 d_w to a nearly uniform distribution.

(ii) For the flip-through impact, the ratio of the maximum total force and the maximum quasi-hydrostatic force is around 11, which is more than two times higher comparing to the slightly-breaking case. The largest pressure occurs at $z = 0.25$ m with a value of $38.31\rho gH$, i.e., $9.23\rho g(d + H)$, which is close to $10\rho g(d+H)$ as predicted by Peregrine (2003). The rise time of the maximum pressure is 0.3 ms, i.e., around 1/6 t_r of the slightly-breaking case. The corresponding fall time is 1.0 ms, i.e., around 1/3 t_f of the slightly-breaking case. The large pressure is more localized in both time and space for the flip-through case compared to the slightly-breaking case. The largest vertical acceleration of the present flip-through case is $1358g$, which occurs during the initial impact.

(iii) For the impact with a small trapped air pocket, the maximum total force is around 6.06 times the maximum quasi-hydrostatic force. The negative sub-atmospheric pressure due to the decompression of the trapped air pocket is well captured. The total force oscillates for several cycles after the sub-atmospheric pressure, and it is gradually damped to the quasi-hydrostatic force. The largest pressure occurs at $z = 0.27$ m with a value of around $11.89\rho gH$. The pressure within the air pocket region is much smaller than the largest pressure. The behaviour of the largest pressure is similar to the flip-through impact with very short rise and fall times, i.e., $t_r = 0.4$ ms and $t_f = 0.5$ ms.

(iv) For the impact with a large trapped air pocket, the maximum total force is around 9.93 times the maximum quasi-hydrostatic force. The compression and expansion of the air pocket results in pressure oscillations, whose amplitude is larger than in the small air pocket case. The maximum pressure is imposed uniformly within the trapped air pocket region, which is around 12.22 ρgH, i.e., less than 1/3 P_{max} of the flip-through case. The rise time is 49 ms and the fall time is 41.8 ms, which are approximately 100 times longer than the flip-through case. The impact with a large air pocket may represent the worst case with regards to the structure due to the long impulse duration and the

large action area. In addition, the pressure oscillations can excite higher-order vibrations for some structures.

(v) For the broken wave impact, the maximum total force is around 3 times the maximum quasi-hydrostatic force. However, the maximum impact pressure around $56.4\rho gH$, which is even larger than the peak flip-through pressure, although the total force is around 8 times smaller than the flip-through case. Therefore, the broken case is able to generate high local pressure on the wall but not such a large total force. Both the broken and flip-through can result in very high local pressure on the wall and cannot be neglected.

As a summary, different types of wave impacts on a vertical wall is highly sensitive to the wave profiles, breaking point and breaking wave height. Therefore, an accurate prediction of the wave shape should be the first priority for the simulations of breaking wave impacts on seawalls. The free surface capture approach and turbulence model in the present study can provide a reference for the same or similar research field.

Declaration of competing interest

The authors would like to state that there is no conflict of interest for this manuscript.

Acknowledgment

The authors would like to thank Dr. Etienne Cheynet for his technical assistance with Matlab. This study was supported in part with computational resources provided by the Norwegian Metacenter for Computational Science (NOTUR), under Project No: NN9372K.

References

Allsop, N., 1999. New design methods for wave loadings on vertical breakwaters under pulsating and impact conditions. Coast. Struct. 99. Spain, Balkemare.
Allsop, N., McKenna, J., Vicinanza, D., Whittaker, T., 1997. New design methods for wave impact loadings on vertical breakwaters and seawalls. Coast. Eng. 1996, 2508–2521.
Bagnold, R., 1939. Interim Report on Wave-Pressure Research. Excerpt from the J. of the Institution of Civil Engineers.
Blackmore, P., Hewson, P., 1984. Experiments on full-scale wave impact pressures. Coast. Eng. 8, 331–346.
Bredmose, H., Bullock, G., Hogg, A., 2015. Violent breaking wave impacts. part 3. effects of scale and aeration. J. Fluid Mech. 765, 82–113.
Bredmose, H., Peregrine, D., Bullock, G., 2009. Violent breaking wave impacts. part 2: modelling the effect of air. J. Fluid Mech. 641, 389–430.
Bullock, G., Obhrai, C., Peregrine, D., Bredmose, H., 2007. Violent breaking wave impacts. part 1: results from large-scale regular wave tests on vertical and sloping walls. Coast. Eng. 54, 602–617.
Chan, E., Melville, W., 1988. Deep-water plunging wave pressures on a vertical plane wall. Proc. R. Soc. Lond. 417, 95–131.
Colagrossi, A., Landrini, M., 2003. Numerical simulation of interfacial flows by smoothed particle hydrodynamics. J. Comput. Phys. 191, 448–475.
Colagrossi, A., Lugni, C., Brocchini, M., 2010. A study of violent sloshing wave impacts using an improved sph method. J. Hydraul. Res. 48, 94–104.
Cooker, M., Peregrine, D., 1991. A model for breaking wave impact pressures. Coast. Eng. 1990, 1473–1486.
Cooker, M., Peregrine, D., 1991. Violent water motion at breaking-wave impact. Coast. Eng. 1990, 164–176.
Cooker, M.J., Peregrine, D., 1995. Pressure-impulse theory for liquid impact problems. J. Fluid Mech. 297, 193–214.
Cuomo, G., Allsop, W., Takahashi, S., 2010. Scaling wave impact pressures on vertical walls. Coast. Eng. 57, 604–609.
Dean, R.G., 1965. Stream function wave theory: validity and application. In: Proceedings Santa Barbara Specialty Conference. ASCE.
Desjardins, O., Moureau, V., Pitsch, H., 2008. An accurate conservative level set/ghost fluid method for simulating turbulent atomization. J. Comput. Phys. 227, 8395–8416.
Faltinsen, O.M., Landrini, M., Greco, M., 2004. Slamming in marine applications. J. Eng. Math. 48, 187–217.
Fries, T.-P., Matthies, H.G., et al., 2003. Classification and Overview of Meshfree Methods. Department of Mathematics and Computer Science, Technical University of Braunschweig.
Gatin, I., 2018. Multiscale Nonlinear and Viscous Numerical Modelling of Wave Impact Loads. PhD Thesis. Ph.D. thesis Faculty of Mechanical Engineering and Naval Architecture, University of Zagreb.
Goda, Y., 1975. New wave pressure formulae for composite breakwaters. Coast. Eng. 1974, 1702–1720.
Gómez-Gesteira, M., Dalrymple, R.A., 2004. Using a three-dimensional smoothed particle hydrodynamics method for wave impact on a tall structure. J. Waterw. Port, Coast. Ocean Eng. 130, 63–69.
Greco, M., Colicchio, G., Faltinsen, O., 2007. Shipping of water on a two-dimensional structure. part 2. J. Fluid Mech. 581, 371–399.
Hattori, M., Arami, A., Yui, T., 1994. Wave impact pressure on vertical walls under breaking waves of various types. Coast. Eng. 22, 79–114.
Holzmann, T., 2017. Mathematics, Numerics, Derivations and Openfoam (R), Holzmann Cfd.
Huang, J., Carrica, P.M., Stern, F., 2007. Coupled ghost fluid/two-phase level set method for curvilinear body-fitted grids. Int. J. Numer. Methods Fluids 55, 867–897.
Jacobsen, N.G., Fuhrman, D.R., Fredsøe, J., 2012. A wave generation toolbox for the open-source cfd library: openfoam®. Int. J. Numer. Methods Fluids 70, 1073–1088.
Jasak, H., 1996. Error Analysis and Estimation for the Finite Volume Method with Applications to Fluid Flows. Ph.D. thesis. Imperial College London (University of London). PhD Thesis.
Jasak, H., 2009. Finite Volume Discretisation with Polyhedral Cell Support. NUMAP-FOAM Summer School Zagreb.
Jasak, H., Gosman, A., 2001. Residual error estimate for the finite-volume method. Numer. Heat Transf. Part B: Fundamentals 39, 1–19.
Jasak, H., Nilsson, H., Rusche, H., Beaudoin, M., Gschaider, B., 2015. Release Notes for foam-extend-3.2.
Jasak, H., Weller, H., Gosman, A., 1999. High resolution nvd differencing scheme for arbitrarily unstructured meshes. Int. J. Numer. Methods Fluids 31, 431–449.
Kirkgöz, M., 1995. Breaking wave impact on vertical and sloping coastal structures. Ocean Eng. 22, 35–48.
Kirkgoz, M.S., 1982. Shock pressure of breaking waves on vertical walls. J. Waterw. Port, Coast. Ocean Div. 108, 81–95.
Kirkgöz, M.S., Aköz, M.S., 2005. Geometrical properties of perfect breaking waves on composite breakwaters. Ocean. Eng. 32, 1994–2006.
Le Méhauté, B., 2013. An Introduction to Hydrodynamics and Water Waves. Springer Science & Business Media.
Lugni, C., Brocchini, M., Faltinsen, O., 2006. Wave impact loads: the role of the flip-through. Phys. Fluids 18, 122101.
Lugni, C., Brocchini, M., Faltinsen, O., 2010. Evolution of the air cavity during a depressurized wave impact. ii. the dynamic field. Phys. Fluids 22, 056102.
Lugni, C., Miozzi, M., Brocchini, M., Faltinsen, O., 2010. Evolution of the air cavity during a depressurized wave impact. i. the kinematic flow field. Phys. Fluids 22, 056101.
Ma, Z., Causon, D., Qian, L., Mingham, C., Gu, H., Ferrer, P.M., 2014. A compressible multiphase flow model for violent aerated wave impact problems. Proc. R. Soc. A Math. Phys. Eng. Sci. 470.
Menter, F.R., 1994. Two-equation eddy-viscosity turbulence models for engineering applications. AIAA J. 32, 1598–1605.
Minikin, R.C.R., 1963. Winds, waves, and maritime structures: studies in harbour making and in the protection of coasts. Griffin.
Mitsuyasu, H., 1967. Shock pressure of breaking wave. Coast. Eng. 1966, 268–283.
Nielsen, K.B., Mayer, S., 2004. Numerical prediction of green water incidents. Ocean Eng. 31, 363–399.
Obhrai, C., Bullock, G., Wolters, G., MÜller, G., Peregrine, H., Bredmose, H., Grüne, J., 2005. Violent wave impacts on vertical and inclined walls: large scale model tests. In: Coastal Engineering *2004*, vol. 4. World Scientific, pp. 4075–4086.
Oumeraci, H., 1994. Review and analysis of vertical breakwater failures—lessons learned. Coastal engineering 22, 3–29.
Oumeraci, H., Klammer, P., Partenscky, H., 1993. Classification of breaking wave loads on vertical structures. J. Waterw. Port, Coast. Ocean Eng. 119, 381–397.
Oumeraci, H., Kortenhaus, A., Allsop, W., de Groot, M., Crouch, R., Vrijling, H., Voortman, H., 2001. Probabilistic Design Tools for Vertical Breakwaters. CRC Press.
Peregrine, D., 2003. Water-wave impact on walls. Annu. Rev. Fluid Mech. 35, 23–43.
Peregrine, D., Bredmose, H., Bullock, G., Obrhai, C., Müller, G., Wolters, G., 2005. Water wave impact on walls and the role of air. In: Coastal Engineering 2004, vol. 4. World Scientific, pp. 4005–4017.
Plumerault, L.-R., Astruc, D., Villedieu, P., Maron, P., 2012. A numerical model for aerated-water wave breaking. Int. J. Numer. Methods Fluids 69, 1851–1871.
Queutey, P., Visonneau, M., 2007. An interface capturing method for free–surface hydrodynamic flows. Comput. Fluids 36, 1481–1510. https://doi.org/10.1002/j.compfluid.2006.11.007.
Roenby, J., Bredmose, H., Jasak, H., 2016. A computational method for sharp interface advection. Open Science 3. https://doi.org/10.1098/rsos.160405.
Svendsen, I.A., Madsen, P., Hansen, J.B., 1978. Wave characteristics in the surf zone. Coast. Eng. 1978, 520–539.
Takahashi, S., Tanimoto, K., Miyanaga, S., 1985. Uplift wave forces due to compression of enclosed air layer and their similitude law. Coast. Eng. Japan 28, 191–206.
Veldman, A.E., Luppes, R., Bunnik, T., Huijsmans, R.H., Duz, B., Iwanowski, B., Wemmenhove, R., Borsboom, M.J., Wellens, P.R., van der Heiden, H.J., et al., 2011. Extreme wave impact on offshore platforms and coastal constructions. In: ASME 2011 30th International Conference on Ocean, Offshore and Arctic Engineering. American Society of Mechanical Engineers, pp. 365–376.
Veldman, A.E., Luppes, R., van der Heiden, H.J., van der Plas, P., Düz, B., Huijsmans, R. H., 2014. Turbulence modeling, local grid refinement and absorbing boundary conditions for free-surface flow simulations in offshore applications. In: ASME 2014

33rd International Conference on Ocean, Offshore and Arctic Engineering. American Society of Mechanical Engineers (pp. V002T08A076–V002T08A076).
Versteeg, H.K., Malalasekera, W., 2007. An Introduction to Computational Fluid Dynamics: the Finite Volume Method. Pearson Education.
Vukčević, V., Jasak, H., Gatin, I., 2017. Implementation of the ghost fluid method for free surface flows in polyhedral finite volume framework. Comput. Fluids 153, 1–19.
Walkden, M., Crawford, A., Bullock, G., Hewson, P., Bird, P., 1996. Wave impact loading on vertical structures. In: Clifford, J.E. (Ed.), Advances in Coastal Structures and Breakwaters. Thomas Telford, London, pp. 273–286.
Wemmenhove, R., Luppes, R., Veldman, A.E., Bunnik, T., 2015. Numerical simulation of hydrodynamic wave loading by a compressible two-phase flow method. Computers & Fluids 114, 218–231.
Witte, H., 1988. Wave Induced Impact Loading in Deterministic and Stochastic Reflection, vol. 102. Mitt Leichtweiss Inst. Wasserbau.
Wood, D., Peregrine, D., Bruce, T., 2000. Study of wave impact against a wall with pressure-impulse theory. part 1: trapped air. J. Waterw. Port, Coast. Ocean Eng. 126, 182–190.
Zhang, S., Yue, D.K., Tanizawa, K., 1996. Simulation of plunging wave impact on a vertical wall. J. Fluid Mech. 327, 221–254.